

Mass assembly and morphological transformations since $z \sim 3$ from CANDELS

M. Huertas-Company,^{1,2★} M. Bernardi,² P. G. Pérez-González,³ M. L. N. Ashby,⁴
 G. Barro,⁵ C. Conselice,⁶ E. Daddi,⁷ A. Dekel,⁸ P. Dimauro,¹ S. M. Faber,⁹
 N. A. Grogin,¹⁰ J. S. Kartaltepe,¹¹ D. D. Kocevski,¹² A. M. Koekemoer,¹⁰
 D. C. Koo,⁹ S. Mei^{1,13} and F. Shankar¹⁴

Affiliations are listed at the end of the paper

Accepted 2016 July 22. Received 2016 July 22; in original form 2016 May 2

ABSTRACT

We quantify the evolution of the stellar mass functions (SMFs) of star-forming and quiescent galaxies as a function of morphology from $z \sim 3$ to the present. Our sample consists of $\sim 50\,000$ galaxies in the CANDELS fields (~ 880 arcmin²), which we divide into four main morphological types, i.e. pure bulge-dominated systems, pure spiral disc-dominated, intermediate two-component bulge+disc systems and irregular disturbed galaxies. At $z \sim 2$, 80 per cent of the stellar mass density of star-forming galaxies is in irregular systems. However, by $z \sim 0.5$, irregular objects only dominate at stellar masses below $10^9 M_\odot$. A majority of the star-forming irregulars present at $z \sim 2$ undergo a gradual transformation from disturbed to normal spiral disc morphologies by $z \sim 1$ without significant interruption to their star formation. Rejuvenation after a quenching event does not seem to be common except perhaps for the most massive objects, because the fraction of bulge-dominated star-forming galaxies with $M_*/M_\odot > 10^{10.7}$ reaches 40 per cent at $z < 1$. Quenching implies the presence of a bulge: the abundance of massive red discs is negligible at all redshifts over 2 dex in stellar mass. However, the dominant quenching mechanism evolves. At $z > 2$, the SMF of quiescent galaxies above M^* is dominated by compact spheroids. Quenching at this early epoch destroys the disc and produces a compact remnant unless the star-forming progenitors at even higher redshifts are significantly more dense. At $1 < z < 2$, the majority of newly quenched galaxies are discs with a significant central bulge. This suggests that mass quenching at this epoch starts from the inner parts and preserves the disc. At $z < 1$, the high-mass end of the passive SMF is globally in place and the evolution mostly happens at stellar masses below $10^{10} M_\odot$. These low-mass galaxies are compact, bulge-dominated systems, which were environmentally quenched: destruction of the disc through ram-pressure stripping is the likely process.

Key words: galaxies: abundances – galaxies: evolution – galaxies: high-redshift – galaxies: structure.

1 INTRODUCTION

Lying at the centres of dark matter potential wells, galaxies are the building blocks of our Universe. How they assemble their mass and acquire their morphology are two central open questions today. The answer requires a complete understanding of the complex baryonic physics which dominate at these scales. At first order, however, a galaxy is a system that transforms gas into stars. The life of a galaxy is therefore a balance between processes that trigger star formation

by accelerating gas cooling and others which tend to prevent star formation by expelling or heating gas (e.g. Lilly et al. 2013). Stellar mass functions (SMFs) are a key first-order observable which allows one to statistically trace back the formation of stars in the universe. Comparison with predicted SMFs constrains the mechanisms which trigger, enhance or inhibit star formation.

Deep NIR surveys over large areas undertaken in the last years probe the evolution of the SMFs from $z \sim 4$ (e.g. Pérez-González et al. 2008; Ilbert et al. 2013; Muzzin et al. 2013). They have shown that some form of feedback, to avoid the overformation of stars both at the high-mass and low-mass ends, is necessary. Another key result is that the abundance of passive galaxies steadily increases

*E-mail: marc.huertas@obspm.fr

from $z \sim 4$ to $z \sim 0$. The quenching of star formation is therefore a key process in the evolution of baryons. It causes a bimodal colour distribution at least from $z \sim 3$ (e.g. Whitaker et al. 2011) and is probably the main explanation for the decrease of the star formation rate density in the universe (e.g. Madau & Dickinson 2014).

What makes a galaxy quench is still an open and extensively debated question. The evolution of the SMFs of passive and star-forming galaxies suggests that stellar mass (or more generally halo mass) is a fundamental property tightly linked to the star formation activity. The $z \sim 0$ SMF has a *knee* (M^*) around $\sim 10^{10.7} M_{\odot}$, and this mass scale seems to be independent of redshift. Galaxies tend to quench when they reach that characteristic mass (e.g. Peng et al. 2010; Ilbert et al. 2013; Moutard et al. 2016). This *mass quenching process* primarily takes place at $z > 1$ because, at later times, there are more passive than star-forming galaxies with this mass, so mass quenching becomes less relevant. Therefore, at late times, most of the quenching activity happens below $\sim 10^{10.7} M_{\odot}$, and this tends to flatten the low-mass end of the passive galaxy SMF (e.g. Moutard et al. 2016). Since most of these galaxies are satellites, this quenching is generally referred to as *environmental quenching*. Even though this empirical description of quenching has been extremely successful in explaining the global trends, the actual physical mechanisms behind quenching are still largely unconstrained.

SMFs alone do not provide information on how the formation of stars affects galaxy structure. It is however well established that star formation activity is strongly correlated with morphology. Galaxies which live on the main sequence of star formation tend to have a disc-like morphology with low Sérsic indices, while passive galaxies tend to have early-type morphologies and Sérsic indices larger than 2 (e.g. Wuyts et al. 2011). Whether this is a cause or a consequence is not yet known (Lilly & Carollo 2016). Several studies claim that the observed relation between structure and star formation is in fact a consequence of very dissipative quenching processes. A large amount of gas would be driven into the central parts of the galaxies producing a central burst of star formation and therefore a bulge with high central stellar mass density (e.g. Barro et al. 2013, 2015). However, recent evidence suggests that the dominant quenching mechanism at intermediate stellar masses might be simply a shutting off of the gas supply through strangulation (e.g. Peng, Maiolino & Cochrane 2015) without significant morphological transformations even at very high redshifts (e.g. Feldmann et al. 2016). The observed correlation between central stellar mass density and star formation rate could be mostly explained by the fading of the disc after the strangulation event (e.g. Carollo et al. 2014). This would also explain the relative large abundance of fast-rotating passive galaxies in the local universe (see Cappellari 2016 for a review).

Properly quantifying how the joint distribution of morphology and mass evolves might shed new light on which are the main quenching processes. It also provides a new element of comparison with recent numerical and empirical simulations which now predict morphologies and structure (e.g. Vogelsberger et al. 2014). However, there is currently no benchmark measurement of this type. Large surveys such as SDSS ($z \leq 0.25$; Bernardi et al. 2013) and more recently GAMA ($z \leq 0.06$; Moffett et al. 2016) have enabled a good quantification of the morphological dependence of the SMF at low redshift (the larger volume of the SDSS means it is able to probe rarer higher masses than GAMA). Pushing to higher redshift requires better angular resolution over large areas. As a result, there are very few complete studies of the morphological dependence of the SMF at high redshift. Bundy, Ellis & Conselice (2005) made a

first attempt but stopped at $z \sim 0.8$. Most of the studies at higher redshift are based on smaller subsets of objects (e.g. Conselice, Blackburne & Papovich 2005; Buitrago et al. 2013; Mortlock et al. 2011) or broad morphologies (Mortlock et al. 2015). Future space-based wide surveys, such as *Euclid* and WFIRST-AFTA, will clearly be a major step forward. In the meanwhile, the largest area observed by the *Hubble Space Telescope (HST)* both in the optical and infrared is the CANDELS survey (Grogin et al. 2011; Koekemoer et al. 2011). Even though it does not reach the same coverage as ground-based surveys such as UltraVista (McCracken et al. 2012), it probes at high angular resolution the rest-frame optical morphologies of galaxies from $z \sim 3$ with a similar depth to the deepest NIR ground-based surveys. In this sense, it is currently the best available data set for establishing robust constraints on the abundance of different morphologies in the early universe. This is the main purpose of the present work.

In Huertas-Company et al. (2015), we used new deep-learning techniques to estimate the morphologies of all galaxies with $H < 24.5$ in the five CANDELS fields with unprecedented accuracy.¹ We now use these morphologies, together with robust stellar mass estimates from extensive multi-band imaging, to study the evolution of the SMFs of quiescent and star-forming galaxies of different morphologies from $z \sim 3$, for the first time. We then discuss the implications for the dominant quenching processes and morphological transformations. The data on the mass functions are made public so that they can be directly compared with the predictions of different models.

The paper is organized as follows. In Section 2, we describe the data set used as well as the main physical parameters we measure (morphologies, structural parameters, stellar masses, etc.). In Section 3, we describe the methodology used to derive the SMFs. Section 4 discusses their evolution. Finally in Section 5, we discuss the implications for the star formation histories (SFHs) of the different morphologies and the evolution of the quenching mechanisms at different cosmic epochs.

Throughout the paper, we assume a flat cosmology with $\Omega_M = 0.3$, $\Omega_{\Lambda} = 0.7$ and $H_0 = 70 \text{ km s}^{-1} \text{ Mpc}^{-1}$ and we use magnitudes in the AB system. All stellar masses were scaled to a Chabrier (2003) initial mass function (IMF).

2 DATA SET

2.1 Parent sample

Galaxies in the five CANDELS fields (UDS, COSMOS, EGS, GOODS-S, GOODS-N) are selected in the *F160W* by applying a magnitude cut $F160W < 24.5 \text{ mag (AB)}$. The total area is $\sim 880 \text{ arcmin}^2$. We use the CANDELS public photometric catalogues for UDS (Galametz et al. 2013) and GOODS-S (Guo et al. 2013) and soon-to-be-published CANDELS catalogues for COSMOS, EGS (Stefanon et al., in preparation) and GOODS-N (Barro et al., in preparation). The magnitude cut is required to ensure that the availability of morphologies (Huertas-Company et al. 2015) a key quantity for the analysis presented in this work. The stellar mass completeness resulting from this magnitude cut is extensively discussed in Section 2.4 given its importance to derive reliable SMFs.

¹The catalogue is available at http://rainbowx.fis.ucm.es/Rainbow_navigator_public/.

2.2 Structural properties

We use the publicly available 2D single Sérsic fits from van der Wel et al. (2012) to estimate basic structural parameters (radii, Sérsic indices, axial ratios). The fits were done using GALFIT (Peng et al. 2002) on the three NIR images ($F105W$, $F125W$, $F160W$). The expected uncertainty on the main parameters is less than 20 per cent for the magnitude cut applied in this work as widely discussed in van der Wel et al. (2012, 2014).

2.3 Morphological classification

We use the deep-learning morphology catalogue described in Huertas-Company et al. (2015). In brief, the ConvNets-based algorithm is trained with visual morphologies available in GOODS-S and then applied to the remaining four fields. Following the CANDELS classification scheme, we assign five numbers to each galaxy: f_{sph} , f_{disc} , f_{irr} , f_{PS} , f_{Unc} . These measure the frequency with which hypothetical classifiers would have flagged the galaxy as having a spheroid, a disc, presenting an irregularity, being compact (or a point source) and being unclassifiable/unclear. For a given image, ConvNets are able to predict the various f_{type} values with negligible bias on average, scatter of ~ 10 per cent–15 per cent, and fewer than 1 per cent misclassifications (Huertas-Company et al. 2015).

In what follows, we primarily use the H band ($F160W$) since our sample is dominated by galaxies at $z > 1$, where NIR filters probe the optical rest frame. For $z < 1$ galaxies, we also explored the I -band filters ($814W$, $850LP$) but because the classes we define below are quite broad, the classifications do not change significantly (also see Kartaltepe et al. 2015). In addition, as we show below, at low redshifts our classifications match those in the SDSS rather well: morphological k -corrections do not have a big impact on our results.

In this work, we distinguish four main morphological types defined as follows:

- (i) *spheroids* [SPH]: $f_{\text{sph}} > 2/3$ and $f_{\text{disc}} < 2/3$ and $f_{\text{irr}} < 0.1$
- (ii) *late-type discs* [DISC]: $f_{\text{sph}} < 2/3$ and $f_{\text{disc}} > 2/3$ and $f_{\text{irr}} < 0.1$
- (iii) *early-type discs* [DISCSPH]: $f_{\text{sph}} > 2/3$ and $f_{\text{disc}} > 2/3$ and $f_{\text{irr}} < 0.1$
- (iv) *irregulars* [IRR]: $f_{\text{sph}} < 2/3$ and $f_{\text{irr}} > 0.1$.

The thresholds above are somewhat arbitrary but have been calibrated through visual inspection first to make sure that they indeed result in distinct morphological classes (see also Kartaltepe et al. 2014).

In Appendix A, we show some randomly selected postage stamps of the different morphological classes in the COSMOS/CANDELS field sorted by stellar mass and redshift. Slight changes to the thresholds used to define these classes do not affect our main results. The SPH class contains bulge-dominated galaxies with little or no disc: it should be close to the classical elliptical classification used in the local universe. The DISC class is made of galaxies in which the disc component dominates over the bulge (typically Sb-c galaxies). Between both classes lies the DISCSPH class in which there is no clear dominant component: it should include typical S0 galaxies and early-type spirals (Sa). We also distinguish galaxies with clear asymmetry in their light profiles. This category should capture the variety of irregular systems usually observed in the high-redshift universe (e.g. clumpy, chain, tadpole, etc.). This irregular class might contain a wide variety of galaxies with different physical properties since the classification is based on the irregularity of the light profile. Notice that IRR is defined with no condition on f_{disc} ;

therefore, this class can include many late-type discs at low redshifts (i.e. Sds).

We have verified that the different classes have distinct structural properties. Spheroids are more compact, rounder ($b/a \sim 0.8$) and have larger Sérsic indices ($n \sim 4-5$) than all other morphologies at all stellar masses and at all redshifts. On the other extreme, discs are larger, more elongated ($b/a \sim 0.5$) and have Sérsic indices close to 1, as expected. Disc+spheroids systems lie somewhat in between: they have Sérsic indices ~ 2 , but are less compact than the spheroids and have similar axial ratios to discs (in agreement with the visual classification; also see Huertas-Company et al. 2015). Although a detailed analysis of the structural properties of the different morphologies will be presented elsewhere, Appendix B shows that the different morphologies also have different stellar mass bulge-to-total ratios (B/Ts).

2.4 Stellar masses and completeness

Spectral Energy Distribution (SED) fitting is used to estimate photometric redshifts and stellar masses used in this work. The detailed methodology is described in Wuyts et al. (2011, 2012) and Barro et al. (2013, 2014). Therefore, only the main points are discussed here. Photometric redshifts are the result of combining different codes to improve the individual performance. The technique is fully described in Dahlen et al. (2013). Based on the best available redshifts (spectroscopic or photometric), we then estimate stellar mass-to-light ratios from the PEGASE01 models (Fioc & Rocca-Volmerange 1999). For these, we assume solar metallicity, exponentially declining SFHs, a Calzetti et al. (2000) extinction law and a Salpeter (1955) IMF. The M_*/L values are then converted to a Chabrier IMF by applying a constant 0.22 dex shift. The stellar mass is estimated by multiplying the M_*/L value by the Sérsic-based L (from GALFIT 2D fits – see Section 2.2). See also Bernardi et al. (2013, Bernardi et al. 2016) for extensive discussion of the systematics associated with all these choices.

The stellar mass completeness of the sample is estimated following the methodology of Pozzetti et al. (2010) and Ilbert et al. (2013) separately for star-forming and quiescent galaxies. We first compute the lowest stellar mass (M_{lim}^*) which could be observed for each galaxy of magnitude H given the applied magnitude cut ($H < 24.5$): $\log(M_{\text{lim}}^*) = \log(M_*) + 0.4(H - 24.5)$. We then estimate the completeness as the 90th percentile of the distribution of M_{lim}^* , i.e. the stellar mass for which 90 per cent of the galaxies have lower limiting stellar masses. By adopting this threshold, we make sure that at most 10 per cent of the low-mass galaxies are lost in each redshift bin. Fig. 1 shows the distribution of galaxies in our sample in the mass–redshift plane and the adopted stellar mass completeness as a function of redshift for passive and all galaxies. The sample is roughly complete for galaxies above 10^{10} solar masses at $z \sim 3$ and goes down to 10^9 at $z \sim 0.5$ (see also Table 1). As a sanity check, we use an alternative estimate of the stellar mass completeness by taking advantage of the fact that the CANDELS data are significantly deeper than the H -band selected sample used here ($H < 24.5$). We therefore compute in bins of redshift the stellar mass at which 90 per cent of the galaxies in the full CANDELS catalogue are also included in our bright selection. The resulting stellar mass completeness is overplotted in Fig. 1. It agrees reasonably well with the one estimated independently using the methodology by Pozzetti et al. (2010). The largest differences are observed at the high-mass end. It can be a consequence of low statistics in these stellar mass bins. In the following, we will adopt therefore the first

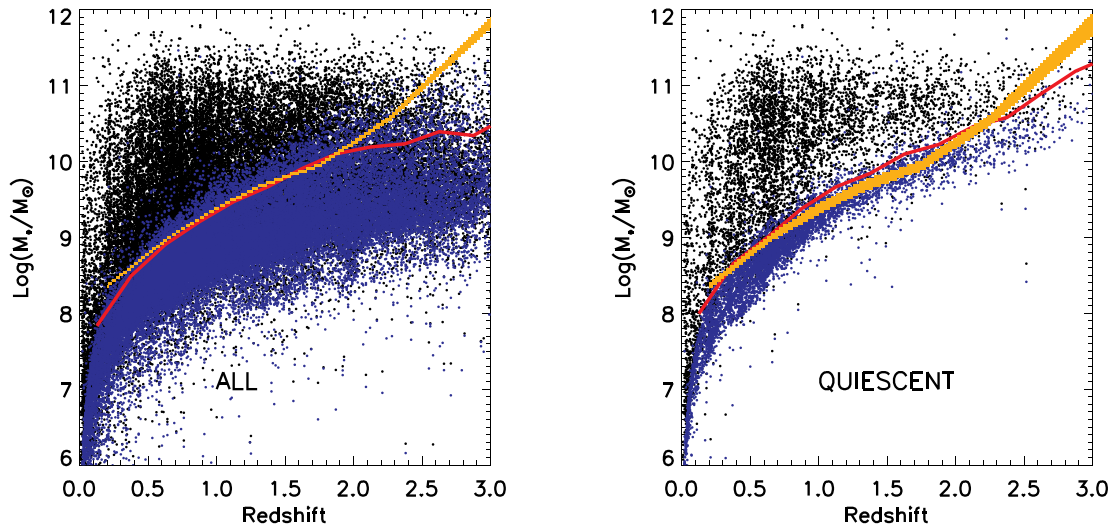


Figure 1. Stellar mass as a function of redshift for all galaxies (left-hand panel) and quiescent galaxies (right-hand panel) for our $H < 24.5$ selected sample. Blue points show the minimum stellar mass which can be observed for a given galaxy computed as explained in the main text. The red line shows the 90th percentile of the distribution of M_{lim} which is the adopted mass completeness in this work (see the text for details). The orange line shows the mass completeness estimated using the full-depth CANDELS catalogue (see the text for details).

estimate, keeping in mind however that at high redshift we might underestimate the completeness.

2.5 Quiescent/star-forming separation

Rest-frame magnitudes (U , V and J) are computed based on the best-fitting redshifts and stellar templates (see Section 2.4) and are then used to separate the passive and star-forming populations as widely used in the previous literature (Whitaker et al. 2012). This colour–colour separation has the advantage of properly distinguishing galaxies reddened by dust from real passive galaxies with old stellar populations.

3 ESTIMATION OF MORPHOLOGICAL SMFs

We use the V_{max} estimator (Schmidt 1968) to derive the SMFs in this work. It has the advantage of being very simple but can easily diverge when the incompleteness becomes too important. For this reason, we restrict our analysis to stellar masses above the thresholds derived in Section 2.4 and quoted in Table 1. Recent works have shown that above the completeness limits, very consistent results are obtained with maximum-likelihood methods (e.g. Ilbert et al. 2013). For simplicity, we restrict our analysis to one single estimator throughout this work.

3.1 Uncertainties

We consider three sources of errors which contribute to the uncertainties on the SMFs. Namely Poisson errors (σ_P), cosmic variance (σ_{CV}) and errors associated with the estimation of stellar masses and photometric redshifts (σ_T). Poisson errors reflect exclusively statistical uncertainties due to the limited number of galaxies in each bin. They are proportional to the square root of the number of objects. Cosmic variance errors are related to the fact that we observe a small area in the sky so our measurements can be affected by statistical fluctuations in the number of galaxies due to the underlying large-scale density fluctuations. Cosmic variance can be computed from the galaxy bias and the dark matter cosmic variance

assuming a cold dark matter (CDM) model. We use the tool of Moster et al. (2011) to estimate the fractional error in density given the size of the CANDELS fields and also their spatial distribution. Finally, uncertainties in stellar mass and redshifts do have an impact on the density of galaxies. Stellar masses are obtained through SED fitting assuming a photometric redshift (spectroscopic redshifts are available for a minority of sources). There are therefore systematic (e.g. template errors, IMF assumptions, SFHs) and statistical errors associated with this methodology.

To estimate this uncertainty, we take advantage of the various measurements of stellar masses and redshifts existing in CANDELS. For example the 3D-HST team has computed an independent set of photometric redshifts and derived stellar masses using the FAST and EAZY codes (Skelton et al. 2014). They used Bruzual & Charlot (2003, hereafter BC03) models and a Chabrier IMF. A comparison of the two should provide an estimate of the errors induced in the SMFs due to errors in redshifts and stellar masses. We therefore generated a set of 50 catalogues by randomly combining stellar masses and photometric redshifts from the CANDELS and 3D-HST catalogues and recomputed the SMFs for each of them. We then measured the scatter in the final 50 SMFs in bins of redshift and stellar mass. This scatter combines the statistical error associated with estimating M_* from fitting noisy photometry to a given set of templates, with the systematic error associated with the fact that the templates used have built-in assumptions about the SFH (bursty or not? dusty or not?, etc.). We note however that this approach certainly underestimates the errors. There is in fact a large overlap in assumptions made, notably the exponentially declining tau models and Calzetti reddening law. Additionally, although the photometric extractions by the 3D-HST and CANDELS teams were done independently, the actual data on which the photometry is based are nearly identical. This is clearly not ideal. Nevertheless, we lump these together and add in quadrature to the other two terms. Hence, to each bin we assign an uncertainty

$$\sigma = \sqrt{\sigma_P^2 + \sigma_{CV}^2 + \sigma_T^2}.$$

Fig. 2 shows the different fractional errors on the number density of galaxies as a function of stellar mass and redshift for the total

Table 1. Best-fitting parameters with single and double Schechter functions to the SMFs of the four morphological types defined in this work. The parameters of the double Schechter are set to -99 whenever a single Schechter was used. Values of -99 are also used when the fit did not converge.

Sample	Redshift	N_{gal}	$\log(M_{\text{complete}})$ (M_{\odot})	$\log(M^*)$ (M_{\odot})	Φ_{\dagger}^* (10^{-3} Mpc^{-3})	α_1	Φ_{\ddagger}^* (10^{-3} Mpc^{-3})	α_2	$\log(\rho_*)$ ($M_{\odot} \text{ Mpc}^{-3}$)
ALL	0.2–0.5	5233	8.43	$10.86^{+0.10}_{-0.10}$	$2.22^{+0.59}_{-0.59}$	$-0.82^{+0.24}_{-0.24}$	$0.45^{+0.15}_{-0.15}$	$-1.60^{+0.00}_{-0.00}$	$8.34^{+0.02}_{-0.02}$
	0.5–0.8	8276	8.94	$10.86^{+0.10}_{-0.10}$	$2.22^{+0.59}_{-0.59}$	$-0.82^{+0.24}_{-0.24}$	$0.45^{+0.15}_{-0.15}$	$-1.60^{+0.00}_{-0.00}$	$8.34^{+0.03}_{-0.03}$
	0.8–1.1	7602	9.29	$11.03^{+0.05}_{-0.05}$	$1.33^{+0.59}_{-0.59}$	$-1.25^{+0.05}_{-0.05}$	$-99.00^{+0.00}_{-0.00}$	$-99.00^{+0.00}_{-0.00}$	$8.24^{+0.03}_{-0.03}$
	1.1–1.5	7099	9.61	$10.97^{+0.05}_{-0.05}$	$0.94^{+0.59}_{-0.59}$	$-1.20^{+0.06}_{-0.06}$	$-99.00^{+0.00}_{-0.00}$	$-99.00^{+0.00}_{-0.00}$	$8.01^{+0.03}_{-0.03}$
	1.5–2	6802	10.02	$10.89^{+0.06}_{-0.06}$	$1.22^{+0.59}_{-0.59}$	$-0.88^{+0.13}_{-0.13}$	$-99.00^{+0.00}_{-0.00}$	$-99.00^{+0.00}_{-0.00}$	$7.95^{+0.03}_{-0.03}$
	2–2.5	4172	10.21	$11.05^{+0.16}_{-0.16}$	$0.41^{+0.59}_{-0.59}$	$-1.19^{+0.26}_{-0.26}$	$-99.00^{+0.00}_{-0.00}$	$-99.00^{+0.00}_{-0.00}$	$7.72^{+0.03}_{-0.03}$
	2.5–3	2147	10.36	$10.90^{+0.18}_{-0.18}$	$0.34^{+0.59}_{-0.59}$	$-0.74^{+0.58}_{-0.58}$	$-99.00^{+0.00}_{-0.00}$	$-99.00^{+0.00}_{-0.00}$	$7.39^{+0.05}_{-0.05}$
SPH	0.2–0.5	0620	8.43	$10.59^{+0.26}_{-0.26}$	$0.75^{+0.24}_{-0.24}$	$-0.25^{+0.45}_{-0.45}$	$0.07^{+0.03}_{-0.03}$	$-1.60^{+0.00}_{-0.00}$	$7.51^{+0.11}_{-0.11}$
	0.5–0.8	1385	8.94	$10.89^{+0.10}_{-0.10}$	$0.91^{+0.18}_{-0.18}$	$-0.51^{+0.21}_{-0.21}$	$0.06^{+0.02}_{-0.02}$	$-1.60^{+0.00}_{-0.00}$	$7.85^{+0.05}_{-0.05}$
	0.8–1.1	1344	9.29	$11.01^{+0.08}_{-0.08}$	$0.48^{+0.09}_{-0.09}$	$-1.00^{+0.07}_{-0.07}$	$-99.00^{+0.00}_{-0.00}$	$-99.00^{+0.00}_{-0.00}$	$7.69^{+0.07}_{-0.07}$
	1.1–1.5	1260	9.61	$10.80^{+0.08}_{-0.08}$	$0.46^{+0.08}_{-0.08}$	$-0.78^{+0.11}_{-0.11}$	$-99.00^{+0.00}_{-0.00}$	$-99.00^{+0.00}_{-0.00}$	$7.42^{+0.05}_{-0.05}$
	1.5–2	1206	10.02	$10.52^{+0.08}_{-0.08}$	$0.59^{+0.04}_{-0.04}$	$0.24^{+0.27}_{-0.27}$	$-99.00^{+0.00}_{-0.00}$	$-99.00^{+0.00}_{-0.00}$	$7.34^{+0.05}_{-0.05}$
	2–2.5	0692	10.21	$10.76^{+0.17}_{-0.17}$	$0.23^{+0.05}_{-0.05}$	$-0.26^{+0.46}_{-0.46}$	$-99.00^{+0.00}_{-0.00}$	$-99.00^{+0.00}_{-0.00}$	$7.09^{+0.07}_{-0.07}$
	2.5–3	0291	10.36	$10.45^{+0.19}_{-0.19}$	$0.09^{+0.04}_{-0.04}$	$0.74^{+0.93}_{-0.93}$	$-99.00^{+0.00}_{-0.00}$	$-99.00^{+0.00}_{-0.00}$	$6.62^{+0.10}_{-0.10}$
DISC+SPH	0.2–0.5	0394	8.35	$10.31^{+0.10}_{-0.10}$	$0.93^{+0.77}_{-0.77}$	$0.00^{+0.00}_{-0.00}$	$0.64^{+0.53}_{-0.53}$	$-0.78^{+0.20}_{-0.20}$	$7.49^{+0.08}_{-0.08}$
	0.5–0.8	0727	8.86	$10.63^{+0.05}_{-0.05}$	$1.27^{+0.15}_{-0.15}$	$-0.49^{+0.07}_{-0.07}$	$-99.00^{+0.00}_{-0.00}$	$-99.00^{+0.00}_{-0.00}$	$7.69^{+0.06}_{-0.06}$
	0.8–1.1	0568	9.21	$10.73^{+0.06}_{-0.06}$	$0.67^{+0.09}_{-0.09}$	$-0.47^{+0.10}_{-0.10}$	$-99.00^{+0.00}_{-0.00}$	$-99.00^{+0.00}_{-0.00}$	$7.50^{+0.07}_{-0.07}$
	1.1–1.5	0394	9.53	$10.77^{+0.08}_{-0.08}$	$0.29^{+0.04}_{-0.04}$	$-0.35^{+0.14}_{-0.14}$	$-99.00^{+0.00}_{-0.00}$	$-99.00^{+0.00}_{-0.00}$	$7.18^{+0.08}_{-0.08}$
	1.5–2	0271	9.94	$10.77^{+0.12}_{-0.12}$	$0.16^{+0.02}_{-0.02}$	$0.12^{+0.34}_{-0.34}$	$-99.00^{+0.00}_{-0.00}$	$-99.00^{+0.00}_{-0.00}$	$7.00^{+0.09}_{-0.09}$
	2–2.5	0092	10.13	$10.73^{+0.26}_{-0.26}$	$0.04^{+0.01}_{-0.01}$	$0.16^{+0.91}_{-0.91}$	$-99.00^{+0.00}_{-0.00}$	$-99.00^{+0.00}_{-0.00}$	$6.34^{+0.14}_{-0.14}$
	2.5–3	0035	10.28	$99.00^{+0.00}_{-0.00}$	$99.00^{+0.00}_{-0.00}$	$99.00^{+0.00}_{-0.00}$	$-99.00^{+0.00}_{-0.00}$	$-99.00^{+0.00}_{-0.00}$	$99.00^{+0.00}_{-0.00}$
DISCS	0.2–0.5	1430	8.35	$10.25^{+1.97}_{-1.97}$	$0.09^{+6.56}_{-6.56}$	$0.00^{+0.00}_{-0.00}$	$1.48^{+1.03}_{-1.03}$	$-1.12^{+0.05}_{-0.05}$	$7.47^{+0.05}_{-0.05}$
	0.5–0.8	2322	8.86	$10.56^{+0.06}_{-0.06}$	$1.04^{+0.17}_{-0.17}$	$-1.15^{+0.05}_{-0.05}$	$-99.00^{+0.00}_{-0.00}$	$-99.00^{+0.00}_{-0.00}$	$7.62^{+0.04}_{-0.04}$
	0.8–1.1	1826	9.21	$10.80^{+0.08}_{-0.08}$	$0.51^{+0.11}_{-0.11}$	$-1.20^{+0.07}_{-0.07}$	$-99.00^{+0.00}_{-0.00}$	$-99.00^{+0.00}_{-0.00}$	$7.56^{+0.05}_{-0.05}$
	1.1–1.5	1167	9.53	$10.98^{+0.10}_{-0.10}$	$0.15^{+0.04}_{-0.04}$	$-1.27^{+0.09}_{-0.09}$	$-99.00^{+0.00}_{-0.00}$	$-99.00^{+0.00}_{-0.00}$	$7.24^{+0.06}_{-0.06}$
	1.5–2	0780	9.94	$10.85^{+0.16}_{-0.16}$	$0.13^{+0.06}_{-0.06}$	$-0.97^{+0.28}_{-0.28}$	$-99.00^{+0.00}_{-0.00}$	$-99.00^{+0.00}_{-0.00}$	$6.96^{+0.07}_{-0.07}$
	2–2.5	0309	10.13	$11.11^{+0.29}_{-0.29}$	$0.03^{+0.02}_{-0.02}$	$-0.97^{+0.55}_{-0.55}$	$-99.00^{+0.00}_{-0.00}$	$-99.00^{+0.00}_{-0.00}$	$6.55^{+0.15}_{-0.15}$
	2.5–3	0104	10.28	$11.42^{+0.85}_{-0.85}$	$0.01^{+0.01}_{-0.01}$	$-1.01^{+0.80}_{-0.80}$	$-99.00^{+0.00}_{-0.00}$	$-99.00^{+0.00}_{-0.00}$	$6.20^{+0.05}_{-0.05}$
IRREGULARS	0.2–0.5	2673	8.35	$9.87^{+0.43}_{-0.43}$	$0.16^{+0.70}_{-0.70}$	$0.00^{+0.00}_{-0.00}$	$0.76^{+0.51}_{-0.51}$	$-1.60^{+0.00}_{-0.00}$	$7.05^{+0.05}_{-0.05}$
	0.5–0.8	3593	8.86	$10.45^{+0.83}_{-0.83}$	$0.04^{+0.43}_{-0.43}$	$0.00^{+0.00}_{-0.00}$	$0.33^{+0.60}_{-0.60}$	$-1.66^{+0.16}_{-0.16}$	$7.34^{+0.04}_{-0.04}$
	0.8–1.1	3613	9.21	$10.72^{+0.11}_{-0.11}$	$0.26^{+0.70}_{-0.70}$	$-1.62^{+0.09}_{-0.09}$	$-99.00^{+0.51}_{-0.51}$	$-99.00^{+0.00}_{-0.00}$	$7.45^{+0.04}_{-0.04}$
	1.1–1.5	3941	9.53	$10.91^{+0.13}_{-0.13}$	$0.17^{+0.70}_{-0.70}$	$-1.60^{+0.09}_{-0.09}$	$-99.00^{+0.51}_{-0.51}$	$-99.00^{+0.00}_{-0.00}$	$7.45^{+0.04}_{-0.04}$
	1.5–2	4210	9.94	$10.91^{+0.11}_{-0.11}$	$0.28^{+0.70}_{-0.70}$	$-1.39^{+0.17}_{-0.17}$	$-99.00^{+0.51}_{-0.51}$	$-99.00^{+0.00}_{-0.00}$	$7.52^{+0.03}_{-0.03}$
	2–2.5	2819	10.13	$10.86^{+0.08}_{-0.08}$	$0.23^{+0.70}_{-0.70}$	$-1.39^{+0.00}_{-0.00}$	$-99.00^{+0.51}_{-0.51}$	$-99.00^{+0.00}_{-0.00}$	$7.37^{+0.04}_{-0.04}$
	2.5–3	1560	10.28	$11.09^{+0.32}_{-0.32}$	$0.09^{+0.70}_{-0.70}$	$-1.35^{+0.46}_{-0.46}$	$-99.00^{+0.51}_{-0.51}$	$-99.00^{+0.00}_{-0.00}$	$7.18^{+0.05}_{-0.05}$

sample. Cosmic variance dominates the error budget for stellar masses below $\sim 10^{11}$. It is in fact always greater than 10 per cent while Poisson and template fitting errors are generally below ~ 5 per cent. At larger stellar masses, the small number statistics generate an increase in the Poisson and template errors, which can exceed 50 per cent at the very highest masses. In the morphology divided samples, the number of objects is obviously reduced and therefore the statistical errors dominate over cosmic variance effects at all stellar masses. Similar trends are observed when the objects are separated into star-forming and quiescent samples.

3.2 Schechter function fits

The non-parametric V_{max} estimator is fitted with a Schechter or double Schechter model, depending on the sample. Given that our sample is not large, especially when it is divided into different morphological types, we preferentially use a single Schechter fit for $z > 0.8$. Only in the lower redshift bins, where the SMFs reach lower stellar masses and an upturn is observed, do we adopt a double Schechter as done in previous works (Pozzetti et al. 2010; Ilbert et al. 2013; Muzzin et al. 2013). In all cases, we only fit data points above the completeness limit to avoid biases related to the

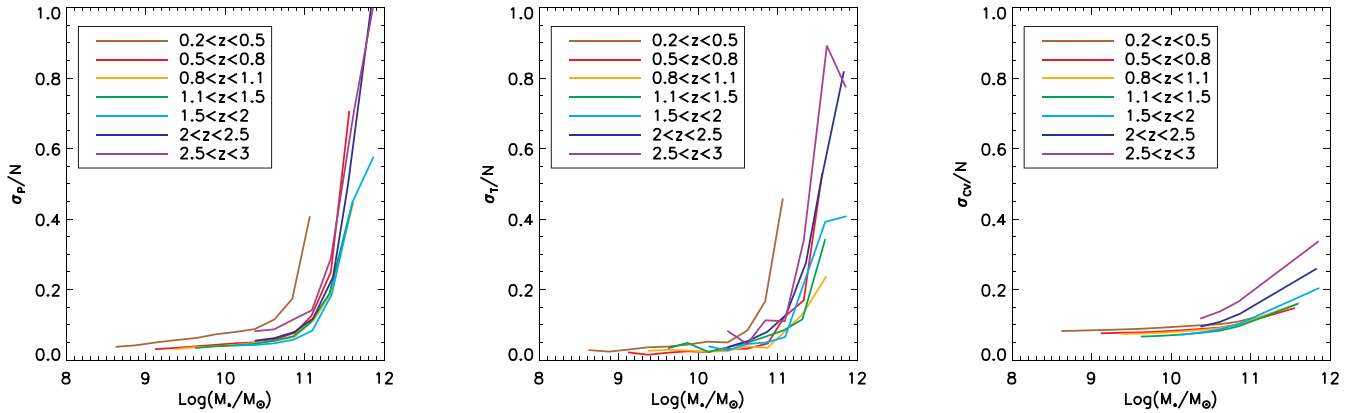


Figure 2. Fractional errors on the number densities of galaxies as a function of stellar mass and redshift for the total sample used in this work. The left-, middle and right-hand columns show Poisson errors, template fitting-related errors and the effects of cosmic variance.

fact that the $1/V_{\max}$ estimator tends to underestimate the number densities beyond the completeness limits.

4 EVOLUTION OF THE MORPHOLOGICAL SMFs

In this section, we discuss the evolution of the SMFs for different morphologies.

4.1 Full sample evolution

Fig. 3 shows the SMFs for each of the four morphological types defined previously; the different panels show results for seven redshift bins. Fig. 4 shows the same information in a different format: each panel shows the evolution of the SMF for a fixed morphological type. The redshift bin sizes were determined by a trade-off between number of objects and lookback time as seen in Tables 1 and 2. The functions are only plotted above the mass completeness limit derived in Section 2.4. Best-fitting parameters are shown in Table 1.

The global mass functions, i.e. not subdivided by morphology (black region in Fig. 3), are also shown and compared with recent measurements in the UltraVista survey by Ilbert et al. (2013) and Muzzin et al. (2013). There is good agreement despite the significantly smaller volume probed by the CANDELS fields. This suggests that our completeness limits are well estimated. Volume effects are mostly visible in the lowest redshift bin, where the CANDELS SMFs show a lack of very massive galaxies.

Before we consider CANDELS in more detail, it is worth remarking on the cyan curve (same in each panel), which shows the SMF in the SDSS from Bernardi et al. (2016). The large volume of the SDSS means Poisson errors are negligible, so the shaded region encompasses the systematic differences between different M_*/L estimates. At low z , the UltraVista measurements are in good agreement with the SDSS; moreover, they lie below it at higher redshifts, as one might expect. In contrast, fig. 5 of Ilbert et al. (2013) shows that their $z \sim 0.5$ SMF lies *above* the $z \sim 0.1$ SDSS SMF, which does not make physical sense. This is because their fig. 5 used the SDSS estimate of Moustakas et al. (2013). Bernardi et al. (2016) discuss why their estimate is to be preferred; note that their work was not motivated by this problem, so the fact that evolution makes better physical sense when their SMF is used as the low-redshift benchmark provides additional support for their analysis. Very briefly, the main reason is that Moustakas et al. (2013) used

SDSS model magnitudes, which underestimate the total luminosity of bright galaxies (Bernardi et al. 2010, 2013; D’Souza, Vegetti & Kauffmann 2015; see especially figs 2 and 3 in Bernardi et al. 2016 and related discussion). This accounts for about half the difference from Bernardi et al.; the remainder is due to M_*/L . Section 4.3 of Bernardi et al. (2016) discusses this in more detail (see, e.g., their figs 14–16). We refer the reader to Bernardi et al. (2016) for a more complete discussion.

If the evolution is driven by star formation (no mergers), then Fig. 4 shows that the stellar mass of galaxies below M^* increases by more than 1 dex in the redshift range $0.5 < z < 3$. More massive galaxies increase their stellar mass by less than 0.5 dex. Therefore, we confirm previous reports of a mass-dependent evolution for the global population. In addition, Table 1 shows that $\log(M^*/M_\odot) \sim 10.85 \pm 0.1$ is approximately independent of redshift.

The key new ingredient of the present work is the evolution at fixed morphology. Morphological evolution and the mass dependence of the dominant morphology are both clearly observed. At $0.2 < z < 0.5$, the population of $\sim M^*$ galaxies ($10 < \log(M_*/M_\odot) < 11$) is essentially uniformly distributed between discs with low bulge fractions, spheroids with large B/Ts and intermediate objects with two components meaning that here is no clear dominant morphology at this mass scale. Above $\log(M_*/M_\odot) = 11$, objects with a clear bulge component tend to dominate the population. Below $10^{10} M_\odot$, the population is basically dominated by objects with small bulges or without. Irregular objects only start dominating the population at $\log(M_*/M_\odot) < 9$. This morphological distribution remains globally unchanged from $z \sim 1$.

Our low-mass SMFs match the local SMFs recently derived in the GAMA survey (Moffet et al. 2016) quite well, as shown in Fig. 4. We overestimate the abundance of irregulars at $\log(M_*/M_\odot) > 10$ compared to them. This is probably a consequence of our definition of irregulars based on the asymmetry of the light profile. It has however little impact on the other morphologies since their abundance is still very low at the high-mass end. The agreement with their work confirms the robustness of our automated classifications.

Above $z \sim 1$, irregular objects start dominating even at higher masses. At $z > 2$, the morphological mix changes radically: there are basically only two types of galaxies at these redshifts – irregulars account for 70 per cent of the objects and bulge-dominated galaxies (spheroids) for the remaining 30 per cent (based on the extrapolations of the Schechter fits). This has a number of interesting implications. First, at these early epochs, the majority of discs are irregular (probably a signature of unstable discs as probed by

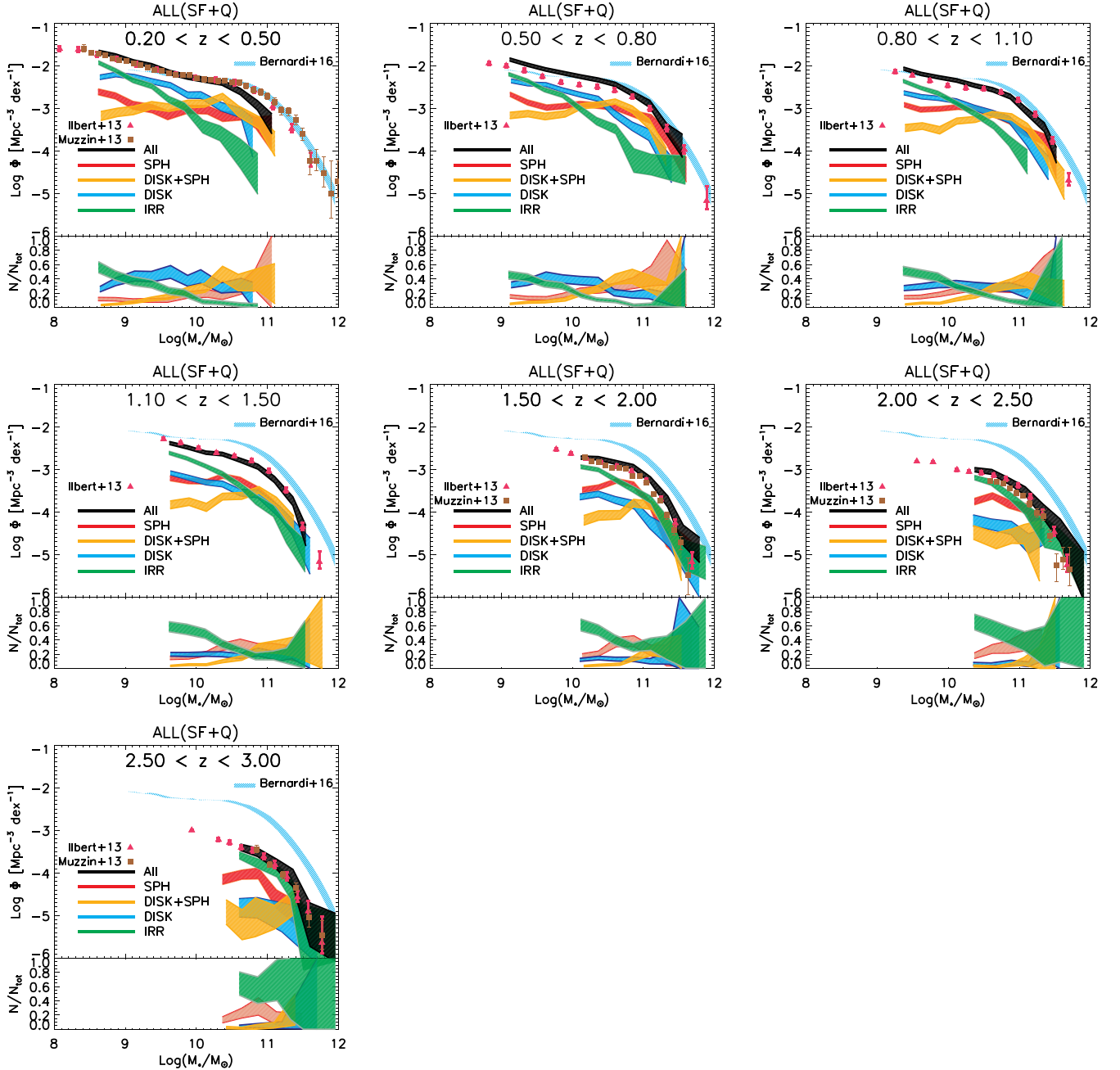


Figure 3. SMFs for four morphological types in different redshift bins as labelled. Red, blue, orange and green shaded regions in the top panels show the number densities of spheroids, discs, disc+spheroids and irregular/clumpy systems, respectively. The bottom panels show the fractions of each morphological type with the same colour code. The black regions show the global SMFs. The pink triangles and brown squares are the measurements by Ilbert et al. (2013) and Muzzin et al. (2013), respectively, in the UltraVista survey. The Muzzin et al. (2013) points are only plotted when their redshift bins are the same as the ones used in this work. We also show for reference in all panels the SMF for all SDSS galaxies (cyan shaded region) from Bernardi et al. (2016).

recent IFU surveys; e.g. Wisnioski et al. 2015). Note that this is not a morphological k -correction effect, since we are probing the optical rest-frame band at this epoch. Secondly, symmetric discs and bulge+disc systems only begin to appear between $z \sim 2$ and $z \sim 1$; objects classified as DISK+SPH account for fewer than 5 per cent of the objects at $z > 2$. This is also observed in the top-right panel of Fig. 4. Discs and disc+spheroid mass functions experience the most dramatic evolution. One might worry that the apparent disappearance of $z \geq 2$ discs is due to surface brightness dimming. This is unlikely though for several reasons. Extensive simulations (e.g.

van der Wel et al. 2014; Kartaltepe et al. 2015) have shown that discs should be detectable at the depth of the CANDELS survey for the magnitude selection used in this work. Also, these are fairly massive galaxies so there is not much room for the presence of a massive disc. In fact, preliminary results of Fig. B1 show a clear correlation between the morphological classification and the stellar mass bulge-to-total ratio which would have been erased if surface brightness dimming was an issue.

These global trends are captured in the top-left panel of Fig. 5 which summarizes the evolution of the stellar mass density

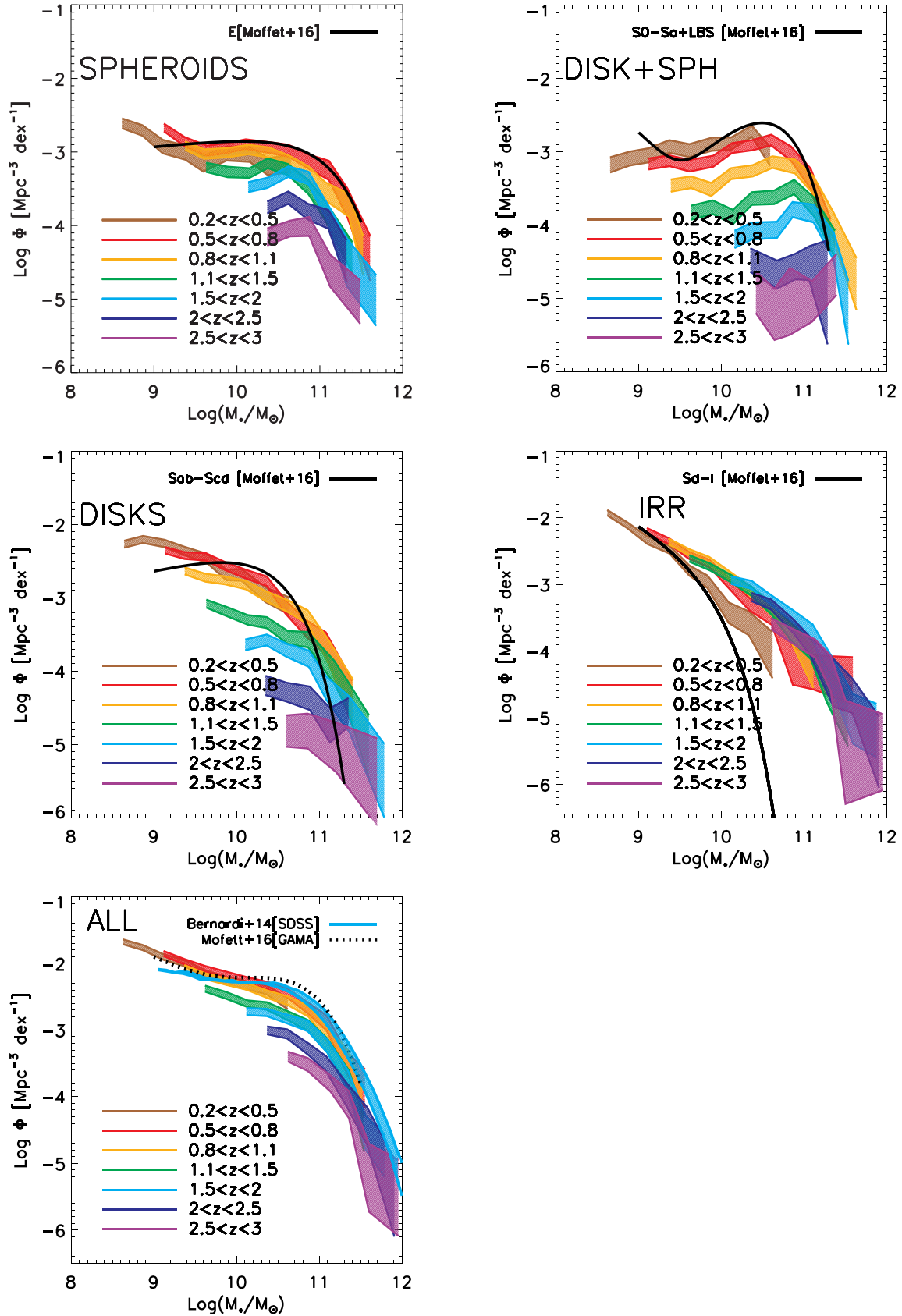


Figure 4. Evolution of the SMFs at fixed morphology. Same as Fig. 3 but binned by morphological type. Each colour shows a different redshift bin. We also overplot the local SMFs from Bernardi et al. (2016) for the total sample and the ones divided by morphology from Moffett et al. (2016) (best-fitting Schechter functions).

Table 2. Best-fitting parameters for a single Schechter function to the star-forming and quiescent SMFs of the four morphological types defined in this work. A = all, S = spheroids, D = discs, DS = discs+spheroids and I = irregulars. Quiescent galaxies at $z > 2.5$ are not fitted because there are too few values above completeness. Quiescent irregulars are also very few. Although the fit works, the mass function is not always well described by a Schechter function. To emphasize this, we have set the error on M^* to 99.9.

S	z	N	Star-forming				Quiescent						
			$L(M_c)$ (M_\odot)	$L(M^*)$ (M_\odot)	Φ_1^* (10^{-3} Mpc^{-3})	α_1	$L(\rho_*)$ ($M_\odot \text{ Mpc}^{-3}$)	N	$L(M_c)$ (M_\odot)	$L(M^*)$ (M_\odot)	Φ_1^* (10^{-3} Mpc^{-3})	α_1	$L(\rho_*)$ ($M_\odot \text{ Mpc}^{-3}$)
A	0.2–0.5	4465	8.43	$10.68^{+0.09}_{-0.09}$	$0.92^{+0.22}_{-0.22}$	$-1.46^{+0.04}_{-0.04}$	$7.85^{+0.05}_{-0.05}$	0768	8.60	$11.01^{+0.14}_{-0.14}$	$0.56^{+0.14}_{-0.14}$	$-1.09^{+0.06}_{-0.06}$	$7.78^{+0.07}_{-0.07}$
	0.5–0.8	7032	8.94	$10.92^{+0.07}_{-0.07}$	$0.83^{+0.17}_{-0.17}$	$-1.46^{+0.04}_{-0.04}$	$8.05^{+0.04}_{-0.04}$	1244	9.04	$10.90^{+0.04}_{-0.04}$	$1.47^{+0.16}_{-0.16}$	$-0.68^{+0.05}_{-0.05}$	$8.02^{+0.06}_{-0.06}$
	0.8–1.1	6743	9.29	$10.93^{+0.06}_{-0.06}$	$0.81^{+0.17}_{-0.17}$	$-1.41^{+0.05}_{-0.05}$	$8.01^{+0.03}_{-0.03}$	0859	9.48	$10.84^{+0.04}_{-0.04}$	$1.17^{+0.11}_{-0.11}$	$-0.40^{+0.08}_{-0.08}$	$7.85^{+0.06}_{-0.06}$
	1.1–1.5	6534	9.61	$10.98^{+0.06}_{-0.06}$	$0.51^{+0.10}_{-0.10}$	$-1.41^{+0.06}_{-0.06}$	$7.86^{+0.03}_{-0.03}$	0565	9.79	$10.73^{+0.02}_{-0.02}$	$0.64^{+0.04}_{-0.04}$	$0.00^{+0.00}_{-0.00}$	$7.53^{+0.05}_{-0.05}$
	1.5–2	6261	10.02	$10.82^{+0.05}_{-0.05}$	$0.93^{+0.15}_{-0.15}$	$-1.00^{+0.12}_{-0.12}$	$7.78^{+0.04}_{-0.04}$	0541	10.16	$10.78^{+0.03}_{-0.03}$	$0.44^{+0.03}_{-0.03}$	$0.00^{+0.00}_{-0.00}$	$7.42^{+0.06}_{-0.06}$
	2–2.5	3961	10.21	$11.29^{+0.16}_{-0.16}$	$0.13^{+0.08}_{-0.08}$	$-1.61^{+0.19}_{-0.19}$	$7.72^{+0.03}_{-0.03}$	0211	10.51	$10.85^{+0.27}_{-0.27}$	$0.18^{+0.08}_{-0.08}$	$-0.56^{+0.86}_{-0.86}$	$7.05^{+0.08}_{-0.08}$
2.5–3	2057	10.36	$11.02^{+0.17}_{-0.17}$	$0.19^{+0.11}_{-0.11}$	$-1.08^{+0.46}_{-0.46}$	$7.33^{+0.05}_{-0.05}$	0090	11.05	$99.99^{+99.99}_{-99.99}$	$99.99^{+99.99}_{-99.99}$	$99.99^{+99.99}_{-99.99}$	$99.99^{+99.99}_{-99.99}$	
S	0.2–0.5	0418	8.43	15.58^{+99}_{-99}	$0.00^{+0.24}_{-0.24}$	$-1.71^{+0.10}_{-0.10}$	$7.00^{+0.09}_{-0.09}$	0202	8.60	$11.04^{+0.22}_{-0.22}$	$0.28^{+0.09}_{-0.09}$	$-0.96^{+0.08}_{-0.08}$	$7.48^{+0.10}_{-0.10}$
	0.5–0.8	0798	8.94	14.37^{+99}_{-99}	$0.00^{+0.02}_{-0.02}$	$-1.77^{+0.08}_{-0.08}$	$7.18^{+0.05}_{-0.05}$	0586	9.04	$10.88^{+0.05}_{-0.05}$	$0.85^{+0.10}_{-0.10}$	$-0.61^{+0.06}_{-0.06}$	$7.76^{+0.07}_{-0.07}$
	0.8–1.1	0872	9.29	$10.86^{+0.14}_{-0.14}$	$0.10^{+0.04}_{-0.04}$	$-1.46^{+0.10}_{-0.10}$	$7.05^{+0.07}_{-0.07}$	0470	9.48	$10.81^{+0.06}_{-0.06}$	$0.62^{+0.07}_{-0.07}$	$-0.41^{+0.10}_{-0.10}$	$7.56^{+0.09}_{-0.09}$
	1.1–1.5	0928	9.61	$10.72^{+0.11}_{-0.11}$	$0.16^{+0.05}_{-0.05}$	$-1.20^{+0.13}_{-0.13}$	$6.98^{+0.06}_{-0.06}$	0331	9.79	$10.52^{+0.08}_{-0.08}$	$0.39^{+0.03}_{-0.03}$	$0.29^{+0.22}_{-0.22}$	$7.18^{+0.08}_{-0.08}$
	1.5–2	0889	10.02	$10.58^{+0.10}_{-0.10}$	$0.27^{+0.05}_{-0.05}$	$-0.38^{+0.30}_{-0.30}$	$6.97^{+0.06}_{-0.06}$	0316	10.16	$10.35^{+0.07}_{-0.07}$	$0.14^{+0.06}_{-0.06}$	$1.68^{+0.48}_{-0.48}$	$7.11^{+0.07}_{-0.07}$
	2–2.5	0568	10.21	$11.00^{+0.29}_{-0.29}$	$0.06^{+0.05}_{-0.05}$	$-1.08^{+0.46}_{-0.46}$	$6.83^{+0.09}_{-0.09}$	0120	10.51	$10.72^{+0.23}_{-0.23}$	$0.13^{+0.02}_{-0.02}$	$-0.14^{+1.02}_{-1.02}$	$6.81^{+0.10}_{-0.10}$
2.5–3	0248	10.36	15.58^{+99}_{-99}	$0.00^{+0.24}_{-0.24}$	$-1.71^{+0.10}_{-0.10}$	$6.20^{+0.15}_{-0.15}$	0039	11.05	$99.99^{+99.99}_{-99.99}$	$99.99^{+99.99}_{-99.99}$	$99.99^{+99.99}_{-99.99}$	$99.99^{+99.99}_{-99.99}$	
DS	0.2–0.5	0233	8.43	$10.53^{+0.12}_{-0.12}$	$0.48^{+0.11}_{-0.11}$	$-0.85^{+0.09}_{-0.09}$	$7.18^{+0.11}_{-0.11}$	0161	8.60	$10.42^{+0.07}_{-0.07}$	$0.94^{+0.13}_{-0.13}$	$-0.17^{+0.13}_{-0.13}$	$7.36^{+0.09}_{-0.09}$
	0.5–0.8	0408	8.94	$10.66^{+0.06}_{-0.06}$	$0.46^{+0.08}_{-0.08}$	$-0.78^{+0.08}_{-0.08}$	$7.28^{+0.09}_{-0.09}$	0319	9.04	$10.63^{+0.05}_{-0.05}$	$0.89^{+0.08}_{-0.08}$	$-0.01^{+0.11}_{-0.11}$	$7.58^{+0.08}_{-0.08}$
	0.8–1.1	0360	9.29	$10.94^{+0.10}_{-0.10}$	$0.24^{+0.05}_{-0.05}$	$-0.82^{+0.10}_{-0.10}$	$7.28^{+0.09}_{-0.09}$	0208	9.48	$10.67^{+0.06}_{-0.06}$	$0.43^{+0.04}_{-0.04}$	$0.29^{+0.18}_{-0.18}$	$7.37^{+0.09}_{-0.09}$
	1.1–1.5	0281	9.61	$11.02^{+0.12}_{-0.12}$	$0.11^{+0.03}_{-0.03}$	$-0.82^{+0.13}_{-0.13}$	$7.02^{+0.09}_{-0.09}$	0113	9.79	$10.57^{+0.08}_{-0.08}$	$0.10^{+0.02}_{-0.02}$	$1.29^{+0.36}_{-0.36}$	$7.00^{+0.11}_{-0.11}$
	1.5–2	0196	10.02	$10.91^{+0.16}_{-0.16}$	$0.08^{+0.02}_{-0.02}$	$-0.38^{+0.34}_{-0.34}$	$6.78^{+0.12}_{-0.12}$	0074	10.16	$10.65^{+0.09}_{-0.09}$	$0.03^{+0.02}_{-0.02}$	$1.64^{+0.62}_{-0.62}$	$6.77^{+0.12}_{-0.12}$
	2–2.5	0081	10.21	$11.21^{+0.48}_{-0.48}$	$0.01^{+0.01}_{-0.01}$	$-1.06^{+0.69}_{-0.69}$	$6.28^{+0.14}_{-0.14}$	0010	10.51	$10.56^{+0.72}_{-0.72}$	$0.00^{+0.02}_{-0.02}$	$1.94^{+4.85}_{-4.85}$	$5.87^{+0.00}_{-0.00}$
2.5–3	0028	10.36	$10.53^{+0.12}_{-0.12}$	$0.48^{+0.11}_{-0.11}$	$-0.85^{+0.09}_{-0.09}$	$6.66^{+0.06}_{-0.06}$	0007	11.05	$99.99^{+99.99}_{-99.99}$	$99.99^{+99.99}_{-99.99}$	$99.99^{+99.99}_{-99.99}$	$99.99^{+99.99}_{-99.99}$	
D	0.2–0.5	1263	8.43	$10.33^{+0.07}_{-0.07}$	$1.21^{+0.23}_{-0.23}$	$-1.17^{+0.05}_{-0.05}$	$7.46^{+0.06}_{-0.06}$	0202	8.60	16.02^{+99}_{-99}	$0.00^{+3.45}_{-3.45}$	$-1.55^{+0.11}_{-0.11}$	$7.18^{+0.08}_{-0.08}$
	0.5–0.8	2162	8.94	$10.66^{+0.08}_{-0.08}$	$0.80^{+0.18}_{-0.18}$	$-1.24^{+0.06}_{-0.06}$	$7.65^{+0.05}_{-0.05}$	0179	9.04	15.81^{+99}_{-99}	$0.00^{+1.22}_{-1.22}$	$-1.54^{+0.14}_{-0.14}$	$7.06^{+0.09}_{-0.09}$
	0.8–1.1	1752	9.29	$10.80^{+0.07}_{-0.07}$	$0.54^{+0.11}_{-0.11}$	$-1.18^{+0.07}_{-0.07}$	$7.59^{+0.04}_{-0.04}$	0084	9.48	$11.52^{+0.58}_{-0.58}$	$0.02^{+0.02}_{-0.02}$	$-1.17^{+0.22}_{-0.22}$	$6.85^{+0.11}_{-0.11}$
	1.1–1.5	1126	9.61	$11.01^{+0.10}_{-0.10}$	$0.14^{+0.04}_{-0.04}$	$-1.30^{+0.09}_{-0.09}$	$7.27^{+0.06}_{-0.06}$	0044	9.79	$11.15^{+0.26}_{-0.26}$	$0.02^{+0.01}_{-0.01}$	$-0.60^{+0.38}_{-0.38}$	$6.48^{+0.16}_{-0.16}$
	1.5–2	0748	10.02	$10.84^{+0.12}_{-0.12}$	$0.13^{+0.04}_{-0.04}$	$-0.96^{+0.21}_{-0.21}$	$6.96^{+0.08}_{-0.08}$	0039	10.16	$10.79^{+0.43}_{-0.43}$	$0.04^{+0.01}_{-0.01}$	$-0.11^{+1.01}_{-1.01}$	$6.36^{+0.13}_{-0.13}$
	2–2.5	0299	10.21	15.81^{+99}_{-99}	$0.00^{+0.05}_{-0.05}$	$-1.76^{+0.43}_{-0.43}$	$6.77^{+0.09}_{-0.09}$	0014	10.51	$11.25^{+0.46}_{-0.46}$	$0.01^{+0.00}_{-0.00}$	$0.07^{+1.28}_{-1.28}$	$6.24^{+0.02}_{-0.02}$
2.5–3	0103	10.36	$10.33^{+0.07}_{-0.07}$	$1.21^{+0.23}_{-0.23}$	$-1.17^{+0.05}_{-0.05}$	$6.32^{+0.07}_{-0.07}$	0002	11.05	$99.99^{+99.99}_{-99.99}$	$99.99^{+99.99}_{-99.99}$	$99.99^{+99.99}_{-99.99}$	$99.99^{+99.99}_{-99.99}$	
I	0.2–0.5	2472	8.43	$10.15^{+0.15}_{-0.15}$	$0.40^{+0.19}_{-0.19}$	$-1.71^{+0.09}_{-0.09}$	$7.11^{+0.05}_{-0.05}$	0192	8.60	$14.48^{+99.9}_{-99.9}$	$0.00^{+0.00}_{-0.00}$	$-2.07^{+0.19}_{-0.19}$	$6.05^{+0.03}_{-0.03}$
	0.5–0.8	3460	8.94	$10.56^{+0.11}_{-0.11}$	$0.31^{+0.11}_{-0.11}$	$-1.66^{+0.07}_{-0.07}$	$7.40^{+0.04}_{-0.04}$	0130	9.04	$16.17^{+99.9}_{-99.9}$	$0.00^{+0.00}_{-0.00}$	$-1.92^{+0.16}_{-0.16}$	$6.21^{+0.18}_{-0.18}$
	0.8–1.1	3532	9.29	$10.72^{+0.10}_{-0.10}$	$0.33^{+0.11}_{-0.11}$	$-1.57^{+0.08}_{-0.08}$	$7.51^{+0.03}_{-0.03}$	0081	9.48	$18.87^{+99.9}_{-99.9}$	$0.00^{+0.00}_{-0.00}$	$-1.57^{+0.21}_{-0.21}$	$6.53^{+0.10}_{-0.10}$
	1.1–1.5	3887	9.61	$10.86^{+0.09}_{-0.09}$	$0.23^{+0.07}_{-0.07}$	$-1.57^{+0.08}_{-0.08}$	$7.50^{+0.04}_{-0.04}$	0048	9.79	$20.15^{+99.9}_{-99.9}$	$0.00^{+0.00}_{-0.00}$	$-1.45^{+0.19}_{-0.19}$	$6.47^{+0.11}_{-0.11}$
	1.5–2	4132	10.02	$10.88^{+0.08}_{-0.08}$	$0.37^{+0.10}_{-0.10}$	$-1.28^{+0.14}_{-0.14}$	$7.54^{+0.03}_{-0.03}$	0065	10.16	$19.21^{+99.9}_{-99.9}$	$0.00^{+0.00}_{-0.00}$	$-1.59^{+0.19}_{-0.19}$	$6.64^{+0.12}_{-0.12}$
	2–2.5	2776	10.21	$10.93^{+0.06}_{-0.06}$	$0.24^{+0.04}_{-0.04}$	$-1.28^{+0.00}_{-0.00}$	$7.41^{+0.05}_{-0.05}$	0038	10.51	$17.85^{+99.9}_{-99.9}$	$0.00^{+0.00}_{-0.00}$	$-1.93^{+0.39}_{-0.39}$	$6.61^{+0.04}_{-0.04}$
	2.5–3	1530	10.36	$11.53^{+0.37}_{-0.37}$	$0.03^{+0.04}_{-0.04}$	$-1.67^{+0.35}_{-0.35}$	$7.37^{+0.04}_{-0.04}$	0023	11.05	$99.99^{+99.99}_{-99.99}$	$99.99^{+99.99}_{-99.99}$	$99.99^{+99.99}_{-99.99}$	$99.99^{+99.99}_{-99.99}$

(integrated over all galaxies with $\log(M_*/M_\odot) \geq 8$). Since this lower limit lies below the completeness limit, the result relies on extrapolating the best Schechter fits to low masses. We first observe the previously reported double-speed growth of the mass density on the full sample (black line) in good agreement with previous measurements. From $z \sim 4$ to 1, the total mass density increases by a factor of ~ 6 . From $z \sim 1$ onwards, the growth flattens: ρ_* at $z = 0$ is larger by only a factor of ~ 2 . As we discuss in the following sections, this is a consequence of both the decrease in the specific

star formation rate below $z \sim 1$ (e.g. Schreiber et al. 2016) and of quenching at large stellar masses.

Regarding the morphological evolution above 10^8 solar masses (resulting from the extrapolation of the best Schechter fits), the key observed trends observed in Fig. 5 are as follows.

(i) At $z > 2$, more than 70 percent of the stellar mass density is in irregular galaxies (see also Conselice et al. 2005). The stellar mass density in irregulars decreases over time from

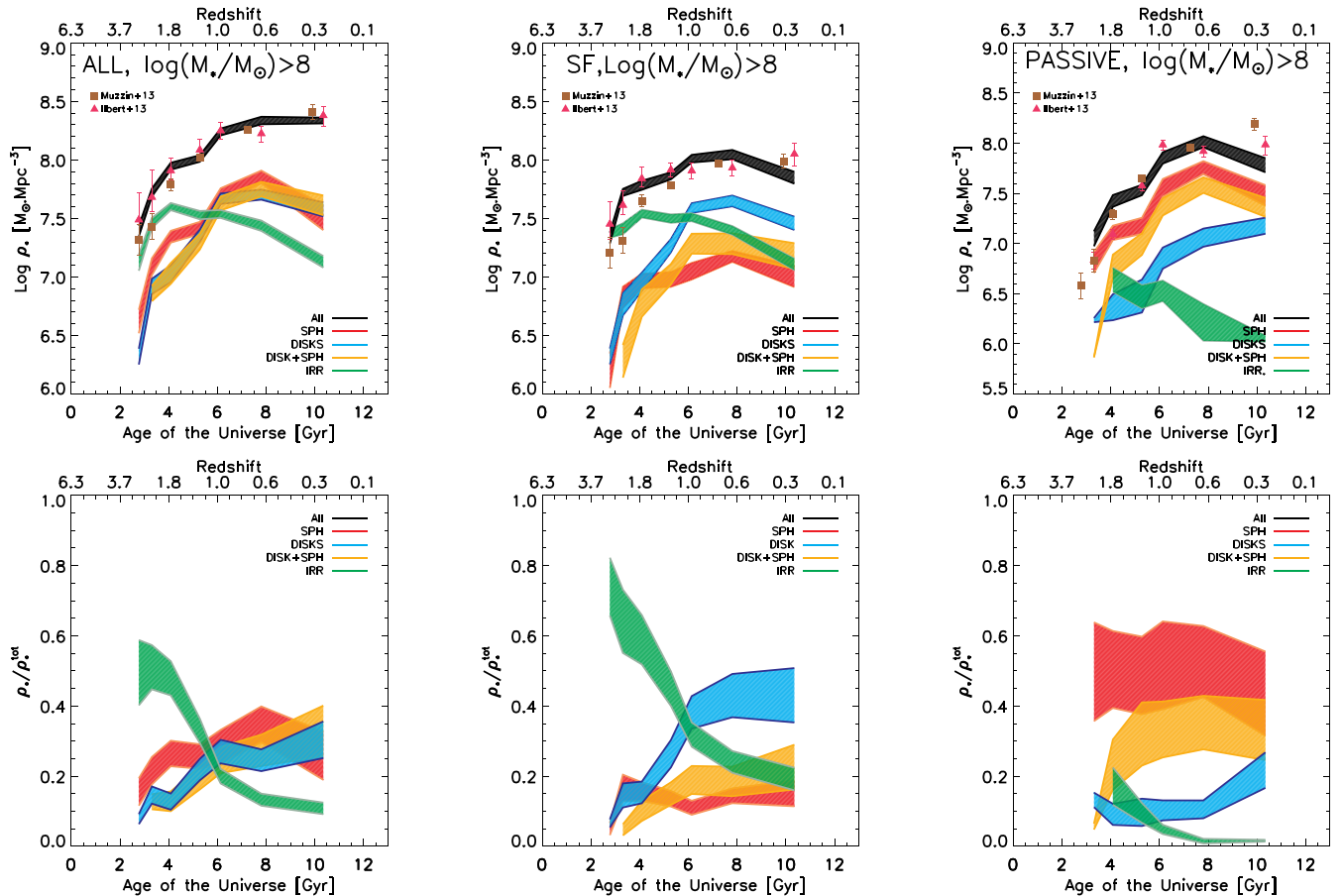


Figure 5. Evolution of the stellar mass density for galaxies with $\log(M_*/M_\odot) > 10^8$. The left-hand panels show the full sample. The middle and right-hand panels show star-forming and quiescent galaxies, respectively. The different colours correspond to different morphologies as labelled. Bottom line are fractions. The pink triangles and brown squares are measurements from Ilbert et al. (2013) and Muzzin et al. (2013).

$\log(\rho_*/M_\odot \text{Mpc}^{-3}) \sim 7.7$ at $z \sim 1.5$ to ~ 7.1 at $z \sim 0.3$. This is clear evidence of morphological transformations as we will discuss in the following sections.

(ii) At $z > 2$, 30 per cent of the stellar mass density is in compact spheroids with large B/T. This suggests that bulge growth at this epoch destroys discs.

(iii) The emergence of *regular discs* (S0a-Sbc) happens between $z \sim 2$ and $z \sim 1$. In this period, the stellar density in both pure discs and bulge+disc systems increases by a factor of ~ 30 .

(iv) Below $z \sim 1$, the stellar mass density is equally distributed among discs, spheroids and mixed systems.

4.2 Evolution of the star-forming population

Fig. 6 shows the evolution of the SMFs of star-forming galaxies as a function of morphological type. To guide the eye, the cyan region (same in all panels) shows the $z \sim 0.1$ SDSS determination as a reference. This curve was obtained by following the analysis of Bernardi et al. (2016), but selecting the subset of objects for which the log of the specific star formation rate determined by the MPA-JHU (e.g. Kauffmann et al. 2003) group is greater than -11 dex.

Table 2 summarizes the best-fitting Schechter function parameters for our CANDELS analysis. In agreement with previous work, the SMF of all star-forming galaxies increases steeply at the low-mass end, and evolves very little at the high-mass end. This is

a consequence of quenching: when star-forming galaxies exceed a critical mass, they quench and so are removed from the star-forming sample (e.g. Peng et al. 2010; Ilbert et al. 2013).

Our new results show that the morphological mix of star-forming galaxies also experiences a pronounced evolution. At $0.2 < z < 0.5$, the typical morphology of a star-forming galaxy differs significantly from that in the full sample. Purely bulge-dominated systems (spheroids) account for ≤ 5 per cent of the objects at all stellar masses. Star-forming galaxies at low redshifts are therefore dominated by regular systems with no pronounced asymmetries and with low bulge fractions (i.e. discs) over two decades in stellar mass ($9 < \log(M_*/M_\odot) < 11$). Irregular discs start to dominate only at very low masses ($\log(M_*/M_\odot) \leq 9$). Bulge+disc systems are also a minority, but account for ~ 40 per cent of the population at stellar masses greater than $\log(M_*/M_\odot) \sim 10.7$. The presence of the bulge component is therefore tightly linked to the star formation activity of the galaxy as widely documented in the recent literature (e.g. Wuyts et al. 2012). As observed for the full sample, this morphological mix seems to have remained rather stable since $z \sim 1$.

At higher redshifts, the relative abundance of irregulars and normal discs is inverted: disturbed systems become the dominant morphological class of star-forming galaxies. The relative abundance steadily increases from $z \sim 1$ to $z \sim 2$. At $z > 2$, irregular systems are almost 100 per cent of the star-forming population. While we confirm a population of star-forming spheroids at $z > 2$ (e.g. van

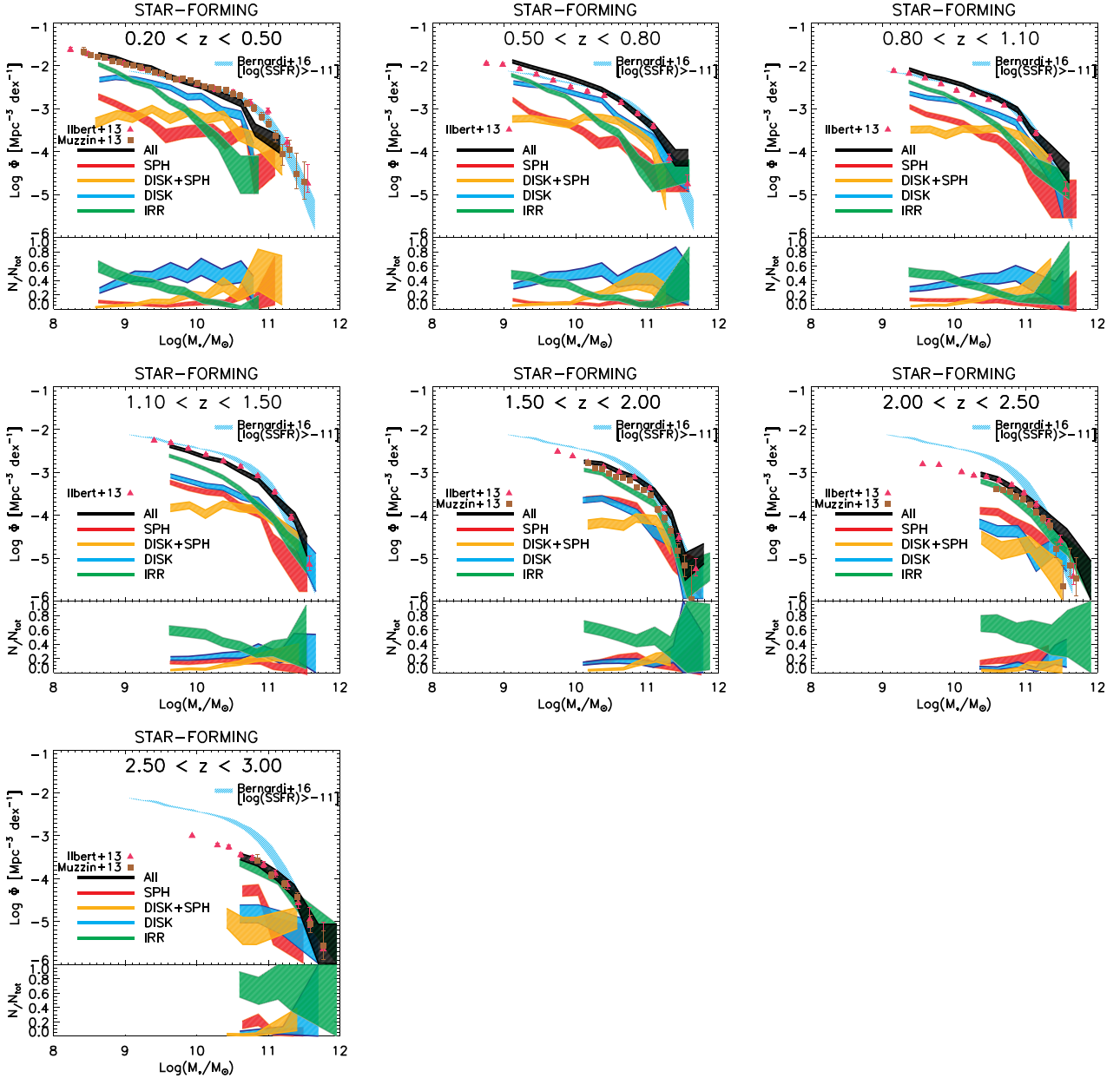


Figure 6. SMFs of star-forming galaxies divided into four morphological types and in different redshift bins as labelled. Red, blue, orange and green shaded regions in the top panels show the number densities of spheroids, discs, disc+spheroids and irregular/clumpy systems, respectively. The black regions show the global mass functions. The pink triangles are the values measured by Ilbert et al. (2013) and the brown squares are the values of Muzzin et al. (2013) in the same redshift bins. The bottom panels show the fractions of each morphological type with the same colour code. The cyan shaded region shows the SMF for the SDSS star-forming galaxies from Bernardi et al. (2016, $\log(\text{SSFR}) > -11$).

Dokkum et al. 2015), they account for only ~ 5 – 10 per cent of the star-forming population at these redshifts. This strongly suggests that bulge formation at these early epochs requires rapid consumption of gas and therefore the quenching of star formation.

These trends are summarized in the middle panel of Fig. 5 which shows the evolution of the integrated stellar mass density of star-forming galaxies with $M_*/M_\odot > 10^8$. The main observed features are as follows.

- (i) Stars are formed in systems with a disc. The abundance of star-forming spheroids is below 10 per cent.
- (ii) There is a transition of the galaxy morphology which hosts star formation. At $z < 1$ – 1.5 , most of the stars in star-forming

systems are in regular discs with low (~ 50 per cent) and intermediate (~ 20 per cent) B/T while at $z > 1.5$ they are predominantly in irregular systems (> 80 per cent).

(iii) The stellar mass density in irregular galaxies decreases with redshift (by a factor of ~ 3); therefore, irregulars are being transformed into other morphologies.

4.3 Evolution of the quiescent population

Fig. 7 shows the evolution of the SMFs of quiescent galaxies as a function of morphological type. We also show in all panels the SMF of quiescent galaxies ($\log(\text{SSFR}) < -11$) in the SDSS based on the recent measurements of Bernardi et al. (2016). The quiescent SMF,

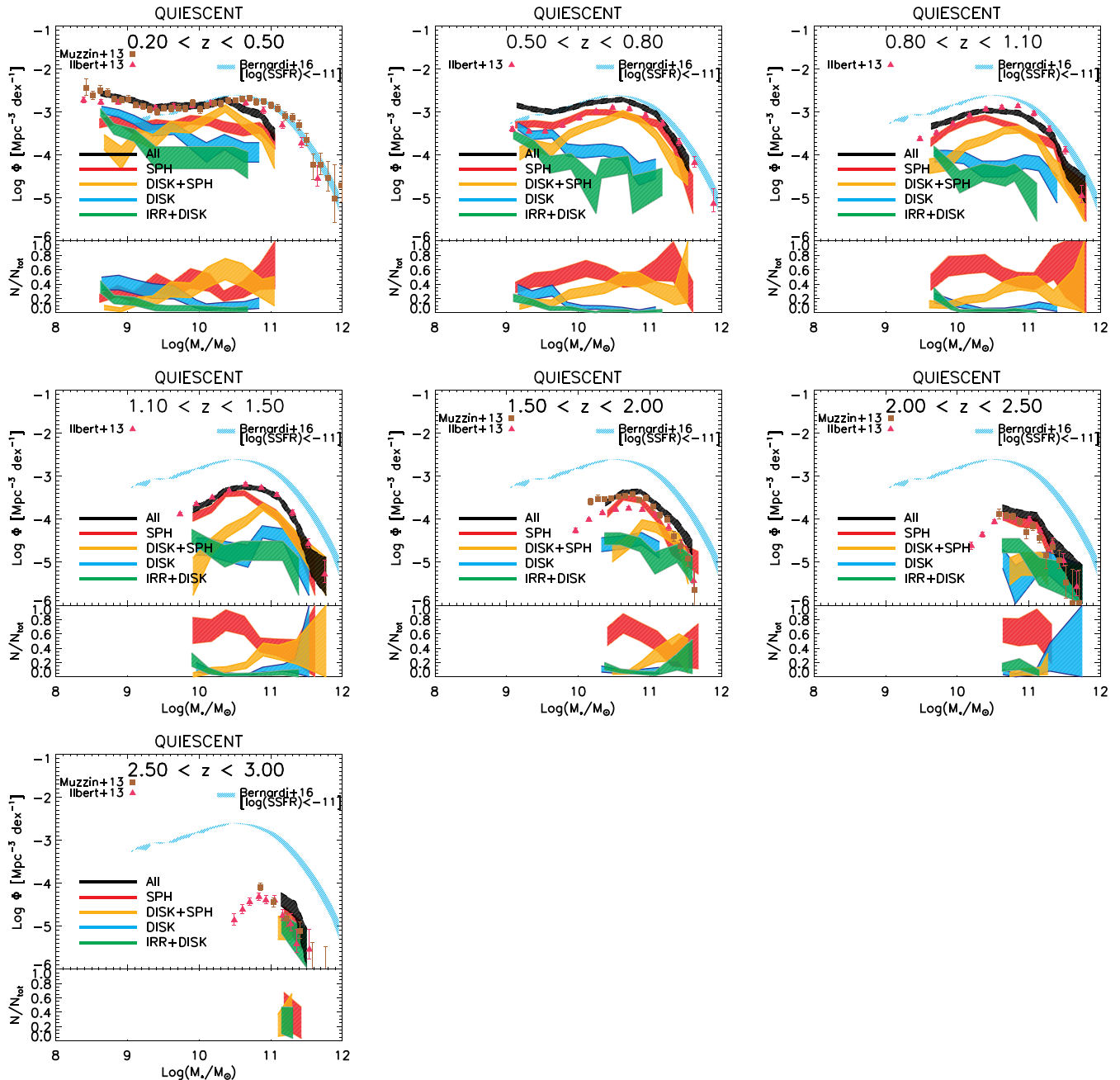


Figure 7. SMFs of quiescent galaxies divided into four morphological types and in different redshift bins as labelled. Red, blue, orange and green shaded regions in the top panels show the number densities of spheroids, discs, disc+spheroids and irregular/clumpy systems, respectively. The black regions show the global mass function. Pink filled triangles and brown squares show the recent SMFs by Ilbert et al. (2013) and Muzzin et al. (2013) in the UltraVista survey respectively. The bottom panels show the fractions of each morphological type with the same colour code. The cyan shaded region shows the SMF for the SDSS quiescent galaxies from Bernardi et al. (2016, $\log(\text{SSFR}) < -11$).

summed over all morphological types, agrees with the one measured in Ilbert et al. (2013). There are some discrepancies, especially in the $0.5 < z < 0.8$ bin, which can be a consequence of both cosmic variance and of a difference in the colours used to select passive galaxies. In any case, the broad evolution trends remain the same. Quiescent galaxies first appear at the high-mass end. The quiescent SMF increases rapidly at the high-mass end up to $z \sim 1$. From $z \sim 1$ to the present, the low-mass population of passive galaxies starts to emerge.

The morphological dissection which our analysis allows provides additional information on how quenching mechanisms affect the morphologies of galaxies. At low redshift, the morphologies of passive galaxies are dominated by two types, pure spheroids and disc+bulge systems. The fraction of quenched late-type spirals is almost negligible (~ 5 per cent), in agreement with measurements in the local universe (Masters et al. 2010). Only below $10^9 M_\odot$ do red disc systems seem to be more abundant. The quenching mechanisms above $10^{10} M_\odot$ are therefore linked to the presence of a bulge.

At $z > 2$, the population of quiescent galaxies is dominated by pure spheroids while the abundance of passive disc+bulge systems (intermediate B/T) is less than 5 per cent at $z \sim 2$. The fraction of disc+bulge systems grows at lower z . This suggests that most of the newly quenched galaxies between $z \sim 2$ and $z \sim 0$ have a disc component.

These trends are also captured in Fig. 5 (which is integrated down to $10^8 M_\odot$). To summarize, the main observed trends are as follows.

(i) ~ 80 – 90 per cent of the stellar mass density of quiescent galaxies is in galaxies with bulges (spheroids and bulge+disc systems) from $z > 2$. Stars in dead galaxies are therefore almost exclusively in systems with a bulge component.

(ii) The relative distribution between the two types changes with time. At $z > 2$, almost all stars are in spheroids while at $z < 1$ stars are equally distributed in discy passive galaxies and spheroids. The stellar mass density in discy passive galaxies increases therefore much faster than in spheroids (a factor of ~ 40 compared to a factor of 4 for spheroids). The majority of newly quenched galaxies between $z \sim 2$ and $z \sim 0.5$ preserve a disc component. This constrains the dominant quenching mechanisms as discussed in Section 5.3.

5 DISCUSSION

The evolution of SMFs can be used to indirectly infer the SFHs of the different morphologies. The evolution also allows an estimate of when different morphologies emerge. We now discuss the implications of our results for morphological transformations and quenching processes at different stellar mass scales from $z \sim 3$ to the present.

5.1 Inferred SFHs at fixed morphology

As is well known, the stellar mass density is the integral of the star formation rate density corrected for the amount of mass-loss:

$$\rho_*(t) = \int_0^t \text{SFRD}(t')(1 - 0.05 \ln(1 + (t - t')/0.3)) dt', \quad (1)$$

where SFRD stands for star formation rate density. The previous equation assumes a parametrization of the return fraction provided by Conroy & Wechsler (2009) with a Chabrier IMF.

Several works have already done this exercise and compared the inferred SFRD evolution with the one obtained from direct measurements, finding different results. Wilkins, Trentham & Hopkins (2008) first reported a discrepancy of ~ 0.6 dex between inferred and direct measurement of the SFHs. Ilbert et al. (2013) revisited this issue with more recent measurements. They found a reasonable agreement with direct measurements from the data compilation of Behroozi et al. (2013), especially at $z < 2$, reducing the previous tensions. We repeat those efforts here, but add morphological information. This enables the first estimates of the formation of stars in different morphologies.

We first assume that the SFRD evolution can be parametrized with a *Lilly–Madau* law as done by Behroozi et al. (2013):

$$\text{SFRD}(z) = \frac{C}{10^{A(z-z_0)} + 10^{B(z-z_0)}}. \quad (2)$$

Then we fit, for each morphological type, an SFRD following the parametrization of equation (2) using equation (1) and the measured of stellar mass densities reported in Fig. 5. The results are shown in Fig. 8. The global inferred SFRD evolution agrees reasonably well with the one derived by Ilbert et al. (2013) using the same

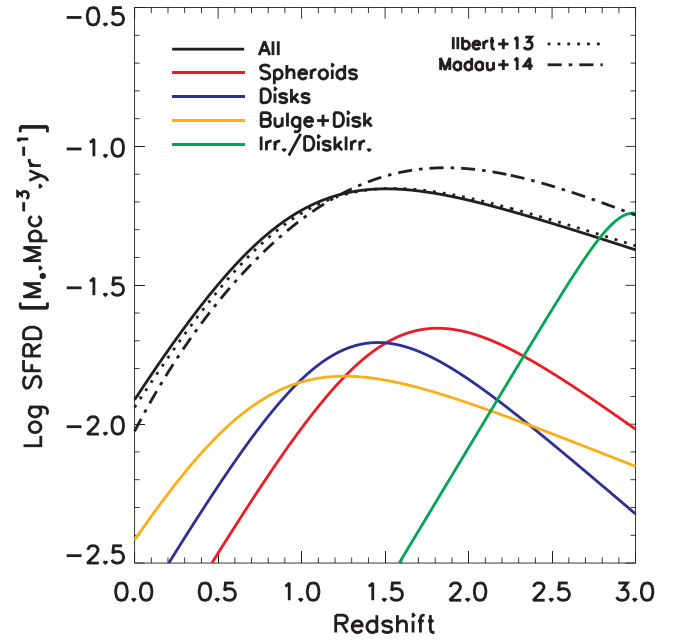


Figure 8. Inferred SFHs for different morphological types. The black solid line shows the global sample and the different colours show the SFHs of different morphologies. The dotted line is the SFRD inferred by Ilbert et al. (2013) on UltraVista following the same methodology. The black dash-dotted line is the most recent compilation of direct measurements by Madau & Dickinson (2014).

methodology but on a completely different data set and with different assumptions on stellar masses. This suggests that the method is robust. With A fixed to -1 , we find best-fitting parameters of $C = 0.11 \pm 0.02$, $B = 0.21 \pm 0.04$ and $z_0 = 0.98 \pm 0.13$. This confirms a peak of star formation activity at $z \sim 2$. Our measurements also agree reasonably well with the most recent compilation of different direct measurements performed by Madau & Dickinson (2014), especially at low redshifts. At $z > 2$, direct measurements estimate an SFRD that is ~ 1.25 times larger than our inferred values.

The interpretation of the SFHs at fixed morphologies is more complex since galaxies can transform their morphologies over time. Hence, the SFRD we infer cannot be directly interpreted as the star formation activity of a single morphological type. Rather, it captures the combined effect of stars formed *in situ* in a given morphology and of new stars which were formed in another morphological type and then merged or transformed. For morphologies with a very low quiescent fraction, it is reasonable to assume that the SFRD will be dominated by *in situ* star formation. However, for morphologies which are mostly quiescent, the inferred history is most probably driven by morphological transformations and mergers. To help in the interpretation of the evolution of the SFRD, Fig. 9 shows the evolution of the quiescent fractions of the different morphological types. As we noted before, it appears that irregulars and discs with low B/T fractions are predominantly star-forming. The quiescent fraction in this population is below 10 per cent. In contrast, the quiescent fraction in (massive) spheroids exceeds ~ 70 per cent at all redshifts. Of course, this is based on the assumption that the SFHs of individual morphologies can indeed be properly parametrized by equation (2).

Nevertheless, the analysis of the SFRDs reveals some interesting first-order trends. There is a clear transition in the dominant morphology hosting star formation. At $z > 2$, star formation mostly takes place in irregular systems. The fact that the best fit exceeds

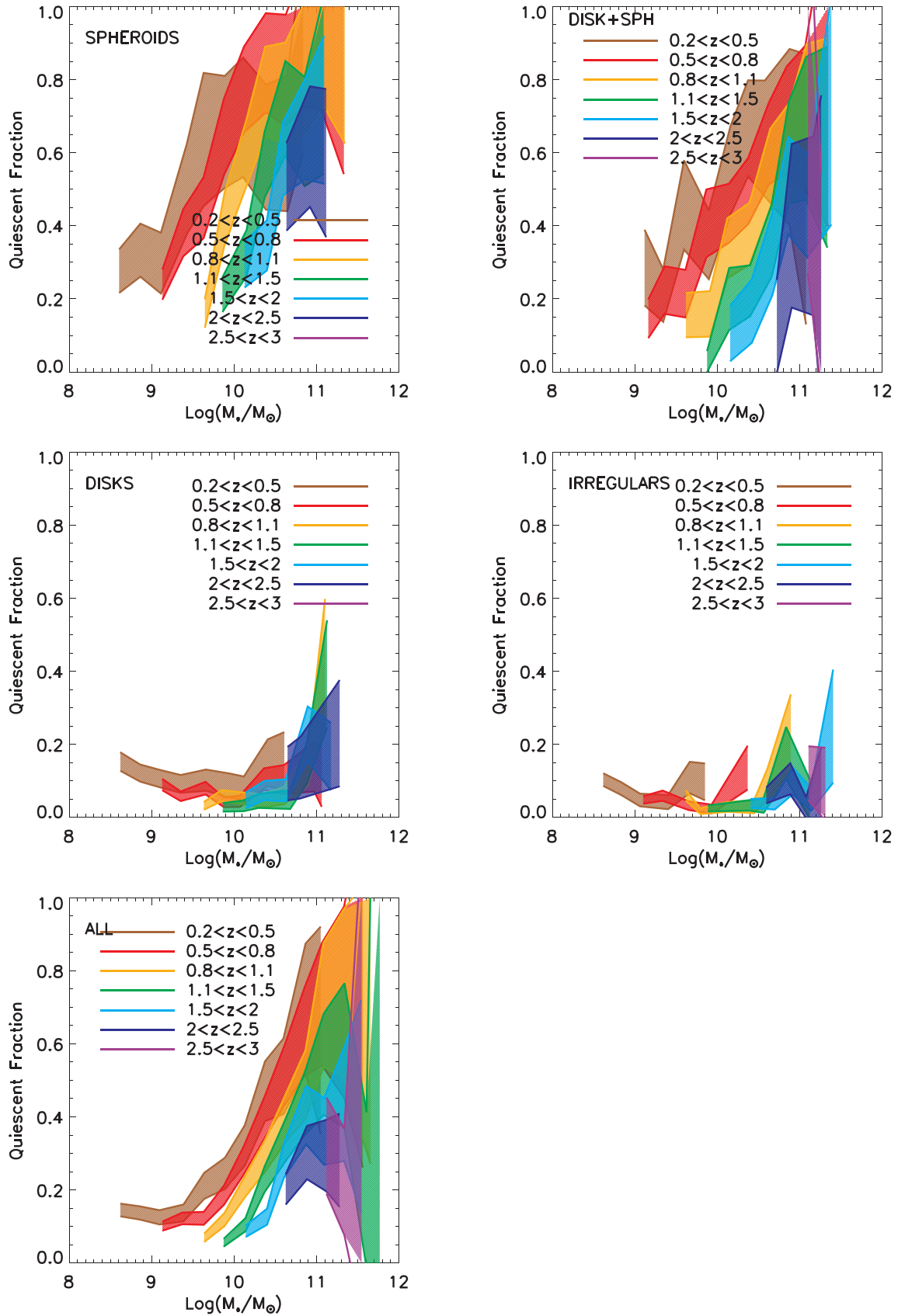


Figure 9. Evolution of the quiescent fraction at fixed morphology. Different colours show different redshift bins as labelled.

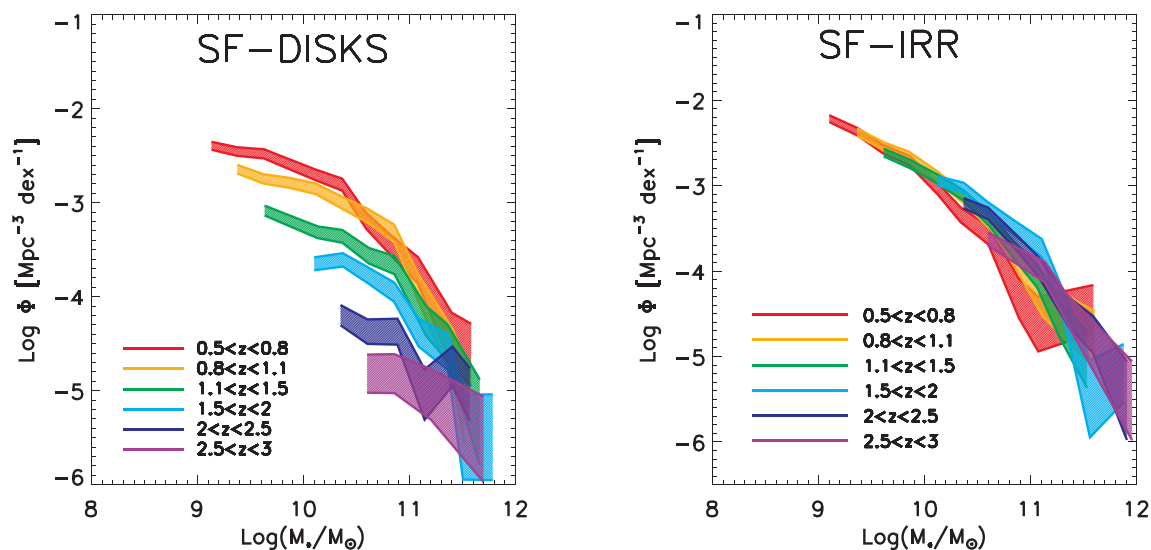


Figure 10. Evolution of the SMF of star-forming galaxies at fixed morphological type. The two dominant morphologies of star-forming galaxies, discs (left) and irregulars (right), are shown.

the global SFRD is clearly an effect of the oversimplification of our model. The SFH of irregulars peaks indeed at $z \sim 2.5\text{--}3$ and sharply decreases thereafter. But this does not mean that they stop forming stars: their quiescent fraction is ≤ 5 per cent at all redshifts. Rather, they must transform into other morphologies. At $z \sim 1.5$, stars are indeed formed in normal symmetric discs both with and without bulge.

Also interesting is that, at high redshift, the SFRD in spheroids is significantly larger than in discs. Again, this does not mean that spheroids are forming more stars than discs, since stars which formed in another morphology and then transformed into spheroids would be credited to spheroids by our parametrization. Since most of spheroids are quiescent, it is likely that the SFH in spheroids is actually dominated by the contribution from transformations. The SFH suggests that the formation of spheroids was most efficient at $z > 2$.

5.2 Constraints on morphological transformations of star-forming galaxies: rejuvenation or continuous star formation?

The SFHs suggest a transition in the morphology where most stars are forming. A more complete understanding requires accounting for the impact of mergers and morphological transformations. Fig. 10 shows the redshift evolution of the SMF of the two morphologies which dominate the star-forming population, i.e. discs (left) and irregulars (right). In the panel on the left, the abundances increase monotonically with time; the opposite is true in the panel on the right. Since the vast majority of irregulars are star-forming, the decrease in the panel on the right indicates that massive irregulars disappear from the irregular class, so they must begin contributing to another morphological class.

What do these objects become? If they continue forming stars, then it is plausible that they transform into symmetric discs. This would be consistent with the low quiescent fractions (< 10 per cent) of both (the irregular and the disc) populations. It would also be qualitatively consistent with the obvious increase with time of the number of normal star-forming discs (left-hand panel of Fig. 10). That is the measured evolution of the disc SMF must result from the

combined effects of morphological transformations and *in situ* star formation. At $z > 1.5$, where irregulars still dominate the population of star-forming galaxies, the evolution in the panel on the right is probably dominated by transformations. Below $z \sim 1$, the reservoir of massive irregular galaxies is exhausted, so from this point on, the evolution becomes dominated by genuine star formation within discs, rather than transformations from irregulars.

This does not actually constrain the individual detailed channels. It does not mean that all star-forming galaxies move straight from an irregular to a pure disc. Only general statistical trends are reflected in the SMF. The individual paths followed by galaxies are necessarily more complex and diverse. As a matter of fact, star formation in a galaxy is not necessarily continuous and galaxies can experience several morphological transformations during their lives. A galaxy can easily destroy a disc, quench and then rejuvenate by rebuilding a disc and going back to the disc SF population (e.g. Hammer et al. 2009; Hopkins et al. 2009). Also a galaxy might appear as an irregular if seen in a merger phase and then go back to the disc population or even become a quenched spheroid. However, this last possibility does not seem to be very common since the evolution of the high-mass end of the spheroid mass function does not significantly evolve. Trayford et al. (2016) recently looked at the individual paths followed by massive galaxies in the EAGLE simulation. They found however that the fraction of rejuvenated discs represents less than 2 per cent of the star-forming population, suggesting that most of the SF galaxies should keep star-forming and experience a gradual morphological transformation as suggested by the global evolution of the SMFs. Separating rejuvenated discs from discs with continuous star formation in our sample requires an accurate age determination of our disc population. While this is not currently possible with the available data (broad- or medium-band photometry), we can try to place some constraints.

As shown in Trayford et al. (2016), most of the rejuvenated galaxies go through a compact quenched phase which lasts ~ 4 Gyr, after which they rebuild a disc. Since rejuvenated objects also build a bulge, once they accrete the disc, an important fraction of them should end up as a star-forming two-component system in our classification system. Thus, to first order, star-forming bulge+disc systems are potential good candidates for being rejuvenated objects.

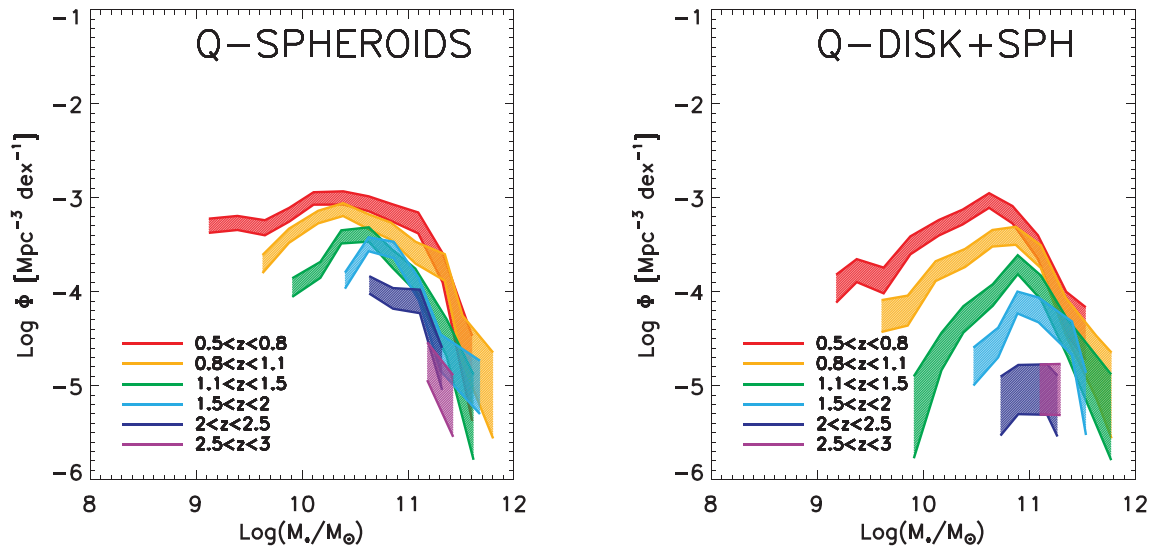


Figure 11. Evolution of the SMF of quiescent spheroids (left) and quiescent disc+spheroids (right).

The fraction of these systems among the star-forming population is ~ 5 per cent which suggests that rejuvenation is not common. Only above $\sim 10^{11} M_{\odot}$, and at low redshifts, does the fraction increase to 30–40 per cent. Major mergers should play an important role at these mass scales (Peng et al. 2010; Cappellari 2016). So these massive systems might result from mergers followed by the accretion of a disc as suggested in numerical simulations (Hopkins et al. 2009). Another possible explanation for this population of star-forming bulge+disc systems is that they are in fact transiting in the other direction, i.e. they are in the process of inside-out quenching (e.g. Tacchella et al. 2015). The fact that they are a small fraction of the population would then suggest that the transitioning phase is short, in line with expectations (e.g. Trayford et al. 2016). We discuss this in the following section.

At the low-mass end, the irregular SMFs show little evidence of evolution. This suggests an equilibrium between the arrival of new systems and galaxy growth followed by morphological transformations. This is expected in a CDM scenario where the halo mass function also evolves little at low masses (e.g. Bocquet et al. 2016). The growth of haloes is indeed compensated by the emergence of new smaller systems. The assumption that these new small haloes will be populated by irregular galaxies initially is in qualitative agreement with the observed mild evolution of the abundance of low-mass irregulars.

5.3 Constraints on quenching processes

The morphological evolution of quiescent and star-forming galaxies constrains the quenching mechanisms which operate at different epochs.

5.3.1 Quenching at M^*

The analysis of the evolution of the global SMFs suggests that galaxies reaching masses close to M^* ($\sim 10^{10.8} M_{\odot}$) tend to quench and populate the quiescent SMF (e.g. Peng et al. 2010; Ilbert et al. 2013). This is now known as mass quenching (i.e. Peng et al. 2010). However, the physical cause of this decrease in star formation is still unclear. It may be a consequence of halo heating, which prevents the inflow of gas that is required to feed further star formation. On the

other hand, quenching may be due to more violent processes such as AGN feedback, or some kind of violent disc instabilities (VDIs), which are expected to have a stronger impact on the morphology.

At low redshift, by studying the metallicity of local quiescent galaxies, Peng et al. (2015) suggested that strangulation might be a dominant process. At high redshift, more violent mechanisms such as VDI might be needed to compactify objects (e.g. Barro et al. 2013, Barro et al. 2015). In Section 4.3, we showed that the quiescent population at $z > 2$ is dominated by spheroids, and that a population of discy passive galaxies emerges at later epochs. In Fig. 11, we show the evolution of the dominant morphologies of quiescent galaxies, i.e. spheroids and disc+spheroids. The plot shows that the SMFs evolve differently. Especially around $10.5 < \log(M_*) < 11$, where mass quenching is expected to be the dominant process, the spheroidal SMF seems to increase with time by a smaller amount than that of disc+spheroids. We quantify this effect in Fig. 12: in this mass range, the number density of pure spheroids evolves little from $z \sim 2$ to the present, whereas that of quiescent galaxies with discs increases ~ 100 times. As discussed in Section 4.3, this is unlikely an observational bias due to cosmic dimming.

One can take a step forward in the interpretation by making the simplistic assumption that pure spheroids are created after some kind of violent dissipative process that destroys the disc and rapidly quenches star formation. Pure SPHs are indeed compact, round and dense (Huertas-Company et al. 2015). Gas-rich major mergers or VDIs followed by some AGN feedback (e.g. Ceverino et al. 2015; Bongiorno et al. 2016) are possible processes. In contrast, discy passive galaxies can be assumed to be predominantly a consequence of a more gradual mechanism related to the lack of available fresh gas (e.g. strangulation; Peng et al. 2015) or morphological quenching (Martig et al. 2009). Then, the evolution observed in Fig. 12 can be interpreted as a signature of a transition in the dominant quenching mechanism. At $2 < z < 3$, violent processes such as mergers and VDIs seem to be rather common channel for quenching since the number of spheroids increases in this period by a factor of ~ 10 . At lower redshift though, VDIs appear to be less common in light of the weak evolution of the abundance of spheroids and the passive evolution of their stellar populations. At $z < 2$, the majority of newly quenched $\sim M^*$ galaxies preserve a passive disc component. Therefore, the most common mass quenching path could be more related

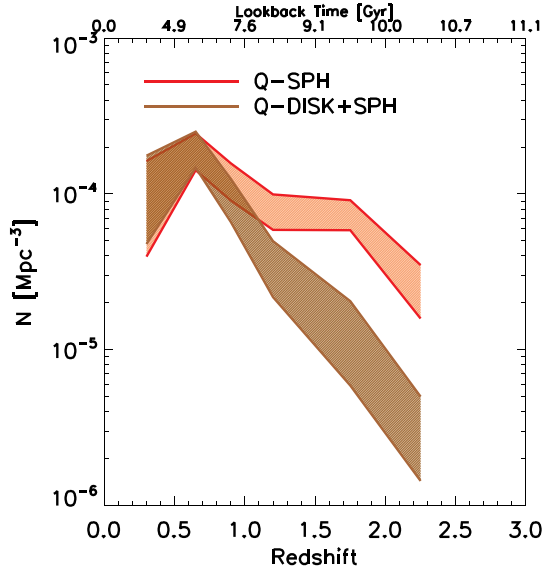


Figure 12. Number density evolution of quiescent galaxies with $10.5 < \log(M_*/M_\odot) < 11$ divided by morphology. Red regions show pure spheroids and brown are early-type discs. The last redshift bin is not shown due to incompleteness.

to some kind of strangulation that provokes an ageing of the stellar populations without significantly altering the morphology. This agrees with Peng et al. (2015). It also means that the population of $\sim M^*$ star-forming bulge+disc systems are probably in the process of quenching from the inside-out (e.g. Tacchella et al. 2015). Although they have already built a bulge, the star formation has not yet ceased. Since this phase is expected to last at most ~ 2 Gyr, this would explain why these objects are so uncommon.

The previous discussion starts from an assumption that the two populations of passive galaxies formed in different processes. This does not need to be true. The fact that galaxies which quenched at later epochs appear larger and less dense can also simply be a consequence of the fact that their star-forming progenitors are also larger given the observed size increase in star-forming galaxies (e.g. van der Wel et al. 2014; Shibuya, Ouchi & Harikane 2015). If so, this would not imply a change in the dominant quenching mechanism. The recent simulations of Feldmann et al. (2016) suggest that the formation of massive quiescent galaxies at very high redshift is also predominantly a consequence of a low amount of gas accretion. Size measurements of star-forming galaxies at $z > 3$ (Shibuya et al. 2015; Ribeiro et al. 2016) also show that the typical effective radii of star-forming galaxies at these redshifts are 1–2 kpc, consistent with the sizes of spheroids at $z < 2-3$. This would imply that the amount of required *compaction* might be less.

5.3.2 Quenching in sub- M^* galaxies

At $z \sim 1.5$, the SMF of quiescent galaxies with stellar masses close to M_* is mostly in place as seen in the bottom panel of Fig. 10 and also in previous works analysing the global mass functions. This means that most of the newly quenched galaxies at $z < 1$ have lower stellar masses, i.e. $\log(M_*/M_\odot) < 10$. They are expected to be predominantly satellite galaxies and the quenching process for these systems is generally known as environmental quenching. The effect of environmental quenching is clearly observed in the low-mass end of the quiescent mass function which begins to turn upwards at $z < 1$.

The analysis of the morphological SMFs derived in this work also reveals interesting properties of the mechanisms of environmental quenching. In fact, at these mass scales, the shape of the SMF of passive bulge+disc systems and spheroids is significantly different. While the abundance of discy systems clearly decreases at the low-mass end (Fig. 11), the one of spheroids tends to increase and mimic the upturn of the global quiescent SMF. Therefore, the low-mass end of the quiescent SMF is in fact predominantly populated by spheroids which are significantly more abundant than disc+bulge systems. This means that the environmental quenching process happening at these mass scales will in general destroy the disc and keep only the central component so that the morphology appears like a roundish bulge-dominated system. Mechanisms like ram-pressure stripping could indeed remove the disc as a satellite galaxy enters a massive halo. Also relevant is that the abundance of red spirals, i.e. passive disc galaxies with no bulge, also increases at $z < 1$ (see Figs 5 and 7). One possible formation mechanism is strangulation as they enter a massive halo as satellites. These two mechanisms seem to coexist at the low-mass end.

We emphasize that this is only a first-order interpretation. A proper quantification of the environments of these low-mass galaxies needs to be undertaken in order to conclude on the effect of environment on quenching. This is beyond the scope of this work and will be explored in the near future.

6 SUMMARY AND CONCLUSIONS

We have studied the evolution of the SMFs of quiescent and star-forming galaxies in the redshift range $0.2 < z < 3$ at fixed morphological type covering an area of ~ 880 arcmin². Our sample consists of $\sim 50\,000$ galaxies with $H < 24.5$. The stellar mass completeness goes from $\log(M_*/M_\odot) \sim 8$ at $z \sim 0.2$ to $\log(M_*/M_\odot) \sim 10.3$ at $z \sim 3$. Galaxies are divided into four main morphological classes based on a deep-learning classification, i.e. pure bulge-dominated spheroids, pure discs, intermediate two-component systems and irregular or disturbed objects. Each morphology has clearly differentiated structural properties. Our main conclusions are summarized below.

(i) Our global SMFs agree with recent measurements from large NIR ground-based surveys. Volume effects are only seen in the lowest redshift bins. We find mass-dependent evolution of the global and star-forming SMF: the low-mass end evolves faster than the high-mass end in agreement with previous work. This is a consequence of *mass quenching* being efficient for galaxies which reach a typical stellar mass of $\log(M_*/M_\odot) \sim 10.8$. The stellar mass density of quiescent galaxies with $\log(M_*/M_\odot) > 8$ increases by a factor of 5 between $z \sim 3$ and $z \sim 1$. At $z < 1$ the passive SMF flattens at the low-mass end; this is usually interpreted a signature of *environment quenching* on satellite galaxies.

(ii) The inclusion of statistical morphological information brings additional insight. See also Fig. 13.

(a) At $z > 2$, the morphological distribution of massive galaxies is bimodal: spheroids and irregulars. All star-forming galaxies are irregulars. Taking into account recent dynamical studies of star-forming objects at $z > 1$, this might be a signature of unstable and turbulent discs. The quiescent galaxies are pure compact spheroids with no clear evidence of a disc component. At these redshifts, the high-mass end of the passive population is building up rapidly. The morphological distribution suggests therefore a violent quenching mechanism as main channel to quench galaxies at $z > 2$. Strong dissipative processes such as very gas rich mergers or VDIs are

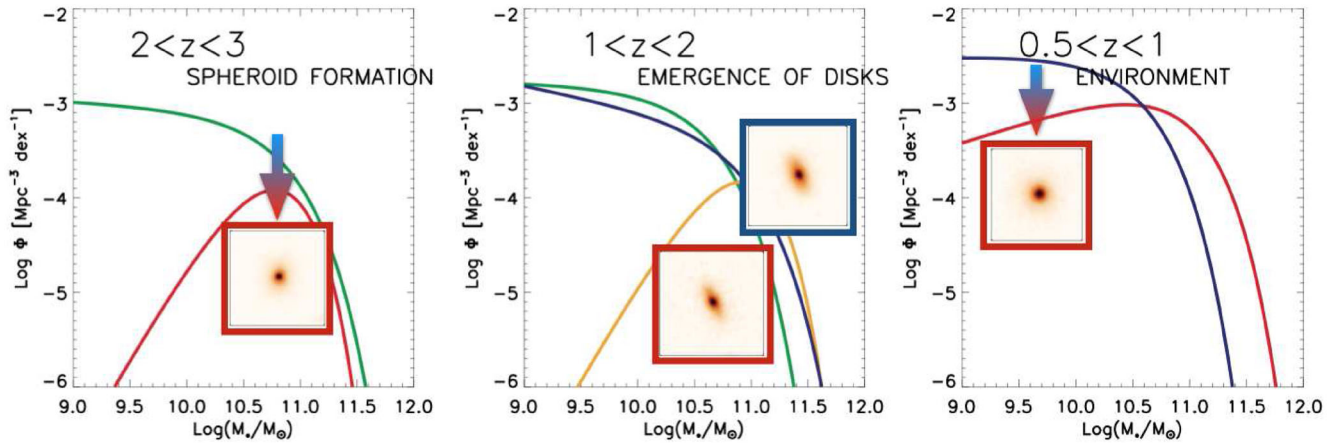


Figure 13. Cartoon summarizing the main statistical trends reported in this work. The green, blue, orange and red curves are the real measured SMFs of irregulars, discs, early-type discs and spheroids, respectively. The arrows indicate quenching. Stamps are typical morphologies emerging at a given epoch. Blue frames for star-forming and red for quiescent.

known to rapidly bring a large amount of gas into the central parts of the galaxy, leading to a massive, compact and dense remnant as observed. Alternatively, they might be the result of quenching of small star-forming systems at higher redshifts.

(b) Within $1 < z < 2$, the majority of *normal* discs observed in the local universe emerge. The SMF of normal star-forming spiral discs evolves rapidly during this time. The evolution is a combination of *in situ* star formation and morphological transformations from irregular discs. At $z \sim 1.5$, star formation occurs primarily in normal spiral discs. To lowest order, this morphological transition does not seem to interrupt star formation. Rejuvenation does not play an important role, although this has to be confirmed with a careful age analysis of the stellar population of late-type discs. The morphological mix of quiescent galaxies also evolves significantly within $1 < z < 2$. Most of the newly massive quenched galaxies in this redshift range have a disc component but with a larger bulge than the star-forming ones. The number density increases 100 times while that of quiescent spheroidals stays roughly constant. The efficiency with which spheroids form decreases and the dominant quenching process does not destroy the disc. This suggests a transition in the main quenching mechanism. Strangulation and/or morphological quenching are possible explanations.

(c) At $z < 1$, there is little evolution of the morphological mix above $10^{10.8} M_{\odot}$. At the highest masses, the abundance of bulgeless systems decreases; nearly 100 per cent of the population has a significant bulge; star-forming objects with a large bulge represent ~ 40 per cent of the population. Galaxies with masses $\sim 10^{10.8} M_{\odot}$ are equally likely to be spheroids as symmetric late- and early-type spirals. Most (95 per cent) passive galaxies are spheroids or early-type spiral/S0 galaxies while most (90 per cent) star-forming galaxies are late-type spirals. Below $\sim 10^{10} M_{\odot}$, irregular objects dominate the star-forming population. Quenching mostly happens at this low-mass end: it creates a population of low-mass bulge-dominated systems and leads to an increase in the fraction of red spirals. This suggests both ram pressure and strangulation as the main quenching mechanisms.

ACKNOWLEDGEMENTS

Thanks to R. Sheth for comments on an early draft. Thanks to the anonymous referee for a constructive and quick report.

REFERENCES

- Barro G. et al., 2013, *ApJ*, 765, 104
 Barro G. et al., 2014, *ApJ*, 791, 52
 Barro G. et al., 2015, preprint ([arXiv:1509.00469](https://arxiv.org/abs/1509.00469))
 Behroozi P. S., Marchesini D., Wechsler R. H., Muzzin A., Papovich C., Stefanon M., 2013, *ApJ*, 777, L10
 Bernardi M., Shankar F., Hyde J. B., Mei S., Marulli F., Sheth R. K., 2010, *MNRAS*, 404, 2087
 Bernardi M., Meert A., Sheth R. K., Vikram V., Huertas-Company M., Mei S., Shankar F., 2013, *MNRAS*, 436, 697
 Bernardi M., Meert A., Sheth R. K., Fischer J.-L., Huertas-Company M., Maraston C., Shankar F., Vikram V., 2016, preprint ([arXiv:1604.01036](https://arxiv.org/abs/1604.01036))
 Bezanson R. et al., 2011, *ApJ*, 737, L31
 Bocquet S., Saro A., Dolag K., Mohr J. J., 2016, *MNRAS*, 456, 2361
 Bongiorno A. et al., 2016, *A&A*, 588, A78
 Bournaud F. et al., 2014, *ApJ*, 780, 57
 Brammer G. B., van Dokkum P. G., Coppi P., 2008, *ApJ*, 686, 1503
 Brammer G. B. et al., 2012, *ApJS*, 200, 13
 Bruce V. A. et al., 2012, *MNRAS*, 427, 1666
 Bruzual G., Charlot S., 2003, *MNRAS*, 344, 1000 (BC03)
 Buitrago F., Trujillo I., Conselice C. J., Haeussler B., 2013, *MNRAS*, 428, 1460
 Bundy K., Ellis R. S., Conselice C. J., 2005, *ApJ*, 625, 621
 Calzetti D., Armus L., Bohlin R. C., Kinney A. L., Koornneef J., Storchi-Bergmann T., 2000, *ApJ*, 533, 682
 Cappellari M., 2016, preprint ([arXiv:1602.04267](https://arxiv.org/abs/1602.04267))
 Carollo C. M. et al., 2014, preprint ([arXiv:1402.1172](https://arxiv.org/abs/1402.1172))
 Chabrier G., 2003, *PASP*, 115, 763
 Conroy C., Wechsler R. H., 2009, *ApJ*, 696, 620
 Conselice C. J., Blackburne J. A., Papovich C., 2005, *ApJ*, 620, 564
 Ceverino D., Dekel A., Tweed D., Primack J., 2015, *MNRAS*, 447, 3291
 Dahlen T. et al., 2013, *ApJ*, 775, 93
 D'Souza R., Vegetti S., Kauffmann G., 2015, *MNRAS*, 454, 4027
 Feldmann R., Hopkins P. F., Quataert E., Faucher-Giguère C.-A., Kereš D., 2016, *MNRAS*, 458, L14
 Fioc M., Rocca-Volmerange B., 1999, preprint ([astro-ph/9912179](https://arxiv.org/abs/astro-ph/9912179))
 Galametz A. et al., 2013, *ApJS*, 206, 10
 Grogin N. A. et al., 2011, *ApJS*, 197, 35
 Guo Y. et al., 2013, *ApJS*, 207, 24
 Hammer F., Flores H., Puech M., Yang Y. B., Athanassoula E., Rodrigues M., Delgado R., 2009, *A&A*, 507, 1313
 Häußler B. et al., 2013, *MNRAS*, 430, 330
 Hopkins P. F., Cox T. J., Younger J. D., Hernquist L., 2009, *ApJ*, 691, 1168
 Huertas-Company M. et al., 2015, *ApJS*, 221, 8
 Ilbert O. et al., 2013, *A&A*, 556, A55

- Kartaltepe J. S. et al., 2014, preprint ([arXiv:1401.2455](https://arxiv.org/abs/1401.2455))
- Koekemoer A. M. et al., 2011, *ApJS*, 197, 36
- Kartaltepe J. S. et al., 2015, *ApJS*, 221, 11
- Kauffmann G. et al., 2003, *MNRAS*, 341, 33
- Lilly S. J., Carollo C. M., 2016, preprint ([arXiv:1604.06459](https://arxiv.org/abs/1604.06459))
- Lilly S. J., Carollo C. M., Pipino A., Renzini A., Peng Y., 2013, *ApJ*, 772, 119
- McCracken H. J. et al., 2012, *A&A*, 544, A156
- Madau P., Dickinson M., 2014, *ARA&A*, 52, 415
- Martig M., Bournaud F., Teysier R., Dekel A., 2009, *ApJ*, 707, 250
- Masters K. L. et al., 2010, *MNRAS*, 405, 783
- Moffett A. J. et al., 2016, *MNRAS*, 457, 1308
- Mortlock A., Conselice C. J., Bluck A. F. L., Bauer A. E., Grützbauch R., Buitrago F., Ownsworth J., 2011, *MNRAS*, 413, 2845
- Mortlock A. et al., 2015, *MNRAS*, 447, 2
- Moster B. P., Somerville R. S., Newman J. A., Rix H.-W., 2011, *ApJ*, 731, 113
- Moustakas J. et al., 2013, *ApJ*, 767, 50
- Moutard T. et al., 2016, *A&A*, 590, A103
- Muzzin A. et al., 2013, *ApJ*, 777, 18
- Peng C. Y., Ho L. C., Impey C. D., Rix H.-W., 2002, *AJ*, 124, 266
- Peng Y., Maiolino R., Cochrane R., 2015, *Nature*, 521, 192
- Peng Y.-j. et al., 2010, *ApJ*, 721, 193
- Pérez-González P. G. et al., 2008, *ApJ*, 675, 234
- Pozzetti L. et al., 2010, *A&A*, 523, A13
- Ribeiro B. et al., 2016, preprint ([arXiv:1602.01840](https://arxiv.org/abs/1602.01840))
- Salpeter E. E. et al., 1955, *ApJ*, 121, 161
- Schmidt M., 1968, *ApJ*, 151, 393
- Schreiber C., Elbaz D., Pannella M., Ciesla L., Wang T., Koekemoer A. M., Rafelski M., Daddi E., 2016, *A&A*, 589, A35
- Shibuya T., Ouchi M., Harikane Y., 2015, *ApJS*, 219, 15
- Skelton R. E. et al., 2014, *ApJS*, 214, 24
- Tacchella S. et al., 2015, *Science*, 348, 314
- Trayford J. W., Theuns T., Bower R. G., Crain R. A., Lagos C. d. P., Schaller M., Schaye J., 2016, *MNRAS*, 460, 3925
- van der Wel A. et al., 2012, *ApJS*, 203, 24
- van der Wel A. et al., 2014, *ApJ*, 788, 28
- van Dokkum P. G. et al., 2015, *ApJ*, 813, 23
- Vogelsberger M. et al., 2014, *MNRAS*, 444, 1518
- Whitaker K. E. et al., 2011, *ApJ*, 735, 86
- Whitaker K. E., van Dokkum P. G., Brammer G., Franx M., 2012, *ApJ*, 754, L29
- Wilkins S. M., Trentham N., Hopkins A. M., 2008, *MNRAS*, 385, 687
- Wisnioski E. et al., 2015, *ApJ*, 799, 209
- Wuyts S. et al., 2011, *ApJ*, 742, 96
- Wuyts S. et al., 2012, *ApJ*, 753, 114

SUPPORTING INFORMATION

Additional Supporting Information may be found in the online version of this article:

suppl_data

(<http://www.mnras.oxfordjournals.org/lookup/suppl/doi:10.1093/mnras/stw1866/-/DC1>).

Please note: Oxford University Press is not responsible for the content or functionality of any supporting materials supplied by the authors. Any queries (other than missing material) should be directed to the corresponding author for the article.

APPENDIX A: MORPHOLOGIES

Figs A1–A4 show postage stamps of a random subset set of galaxies in each of the four main morphological classes used in this work, over a range of different stellar masses and redshifts.

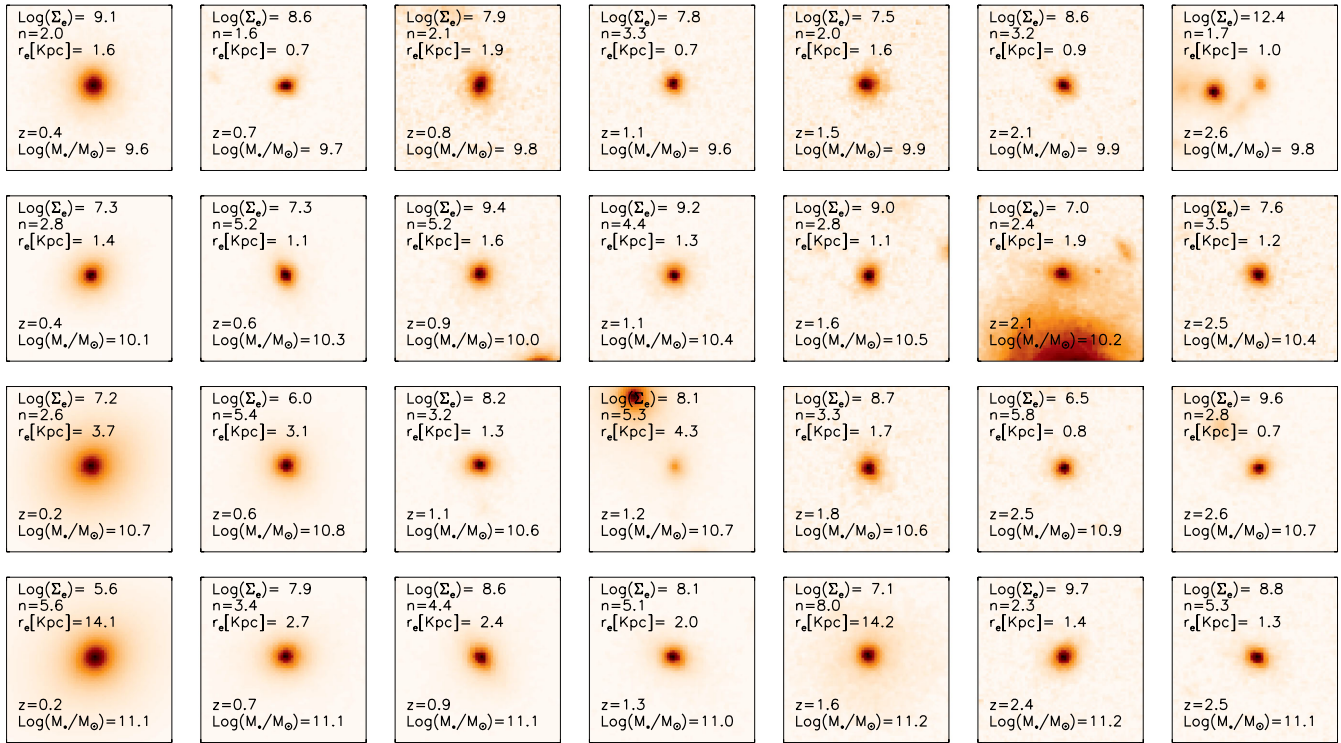


Figure A1. Postage stamps of galaxies classified as spheroids (\sim Es) sorted by increasing stellar mass (vertical direction) and redshift (horizontal direction).

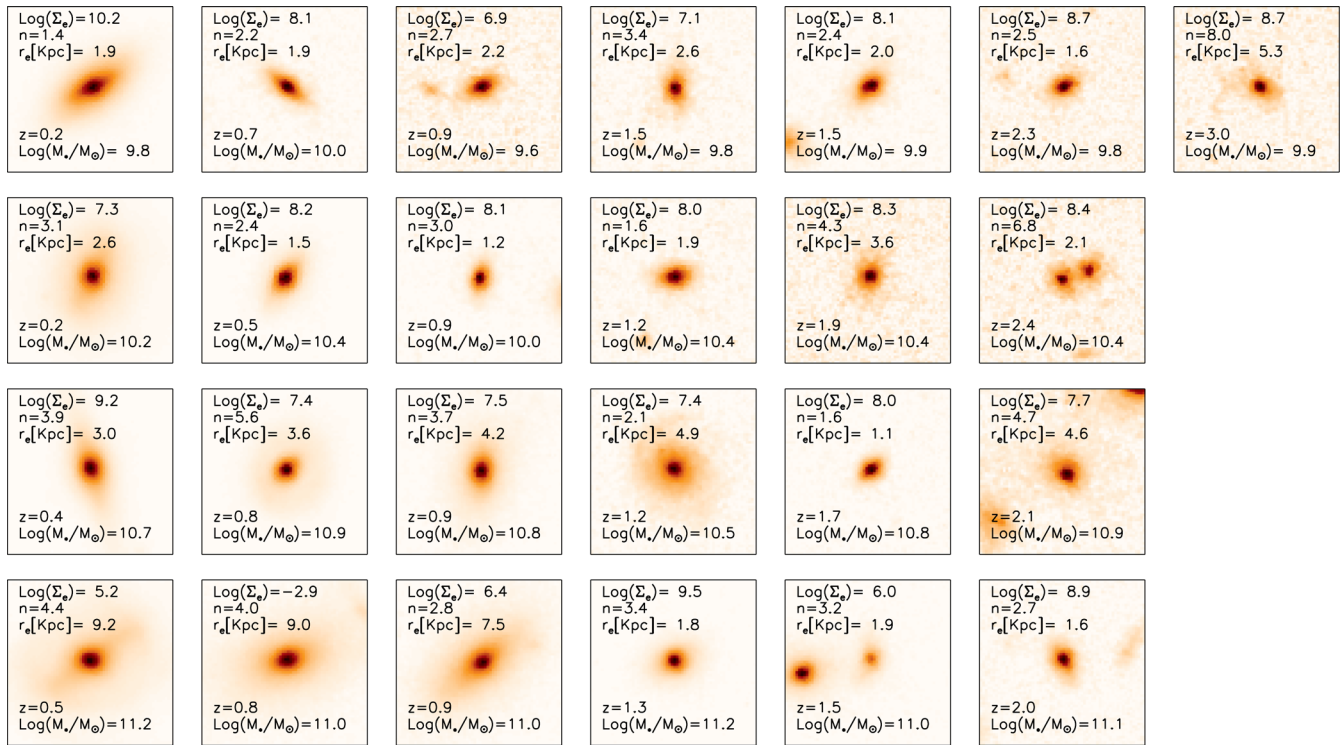


Figure A2. Postage stamps of galaxies classified as disc+spheroids (\sim S0s and early-type spirals) sorted by increasing stellar mass (vertical direction) and redshift (horizontal direction).

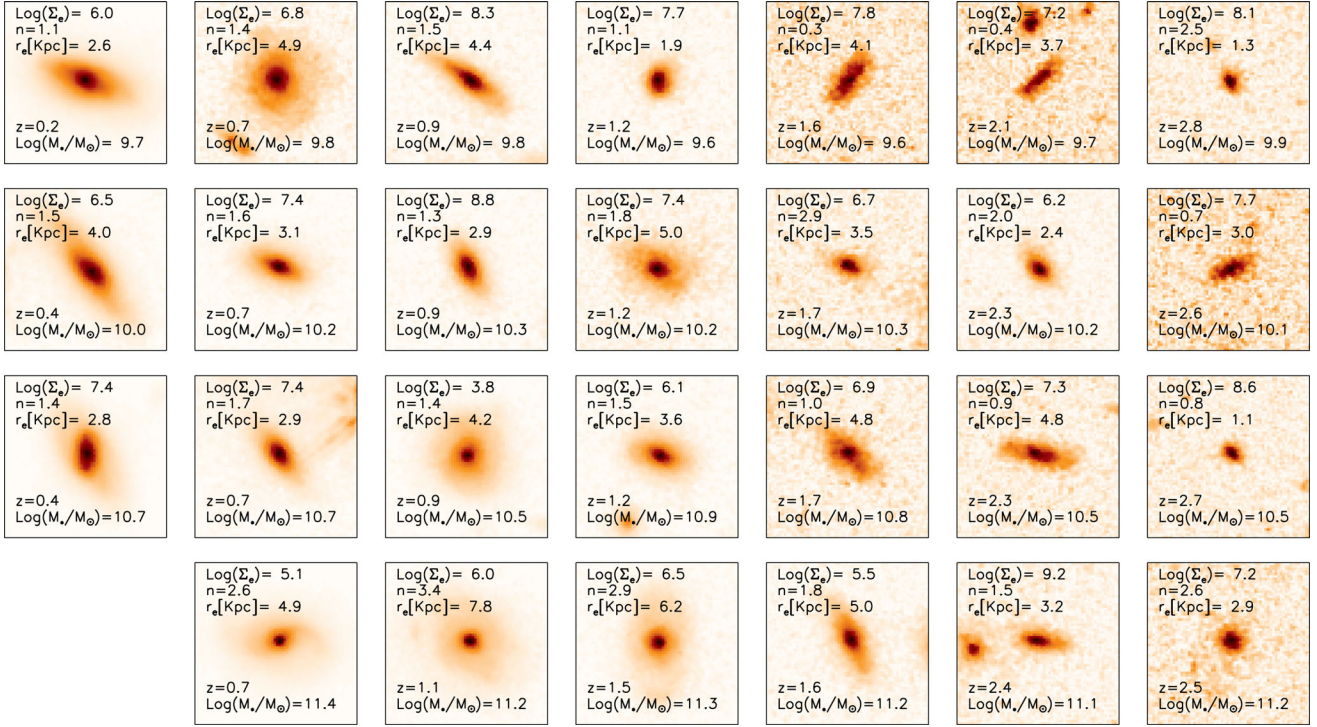


Figure A3. Postage stamps of galaxies classified as discs (\sim late-type spirals) sorted by increasing stellar mass (vertical direction) and redshift (horizontal direction).

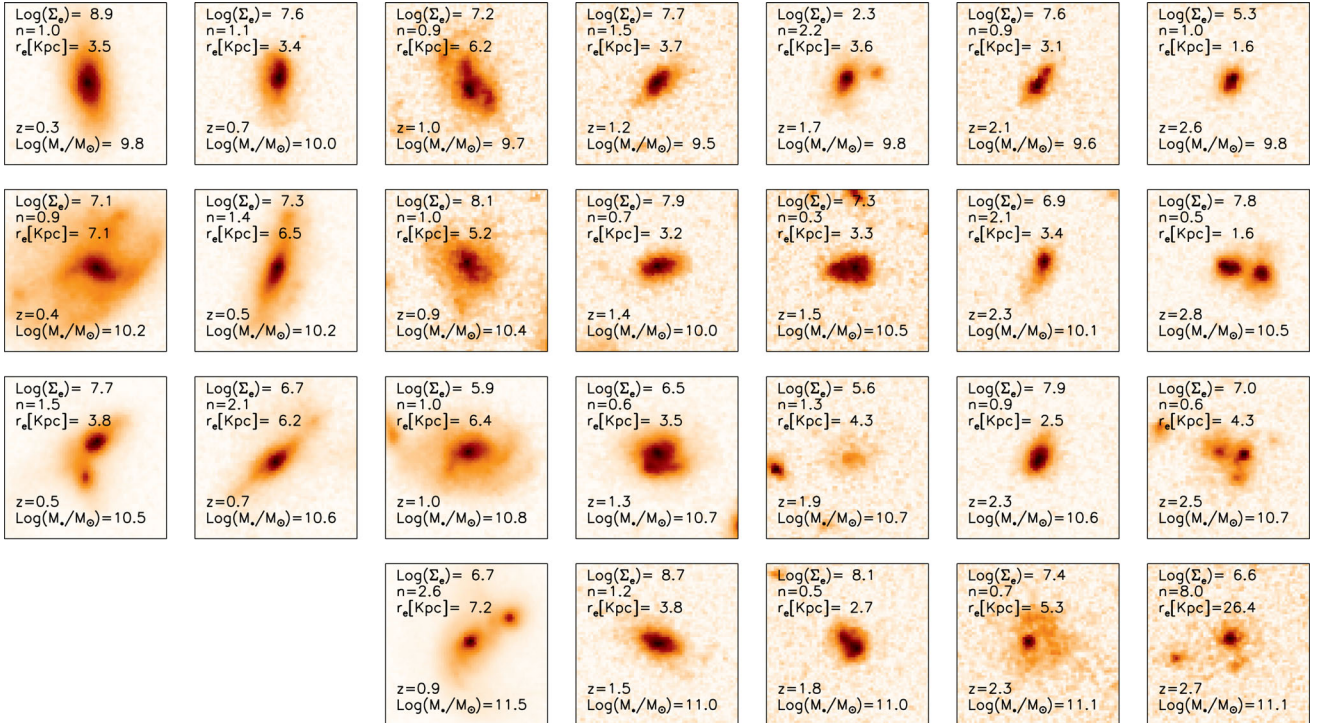


Figure A4. Postage stamps of galaxies classified as irregulars sorted by increasing stellar mass (vertical direction) and redshift (horizontal direction).

APPENDIX B: B/Ts OF DIFFERENT MORPHOLOGIES

As an additional sanity check and given that many models use the stellar mass disc-to-bulge ratio as a proxy for morphology, Fig. B1

shows the stellar mass B/Ts for a subsample of galaxies from our data set. Bulge fractions are obtained by fitting a two-component Sérsic+exponential model on seven *HST* filters (from near UV to NIR) simultaneously using Megamorph (Häußler et al. 2013). Sizes of both components and Sérsic indices of the bulges are allowed to

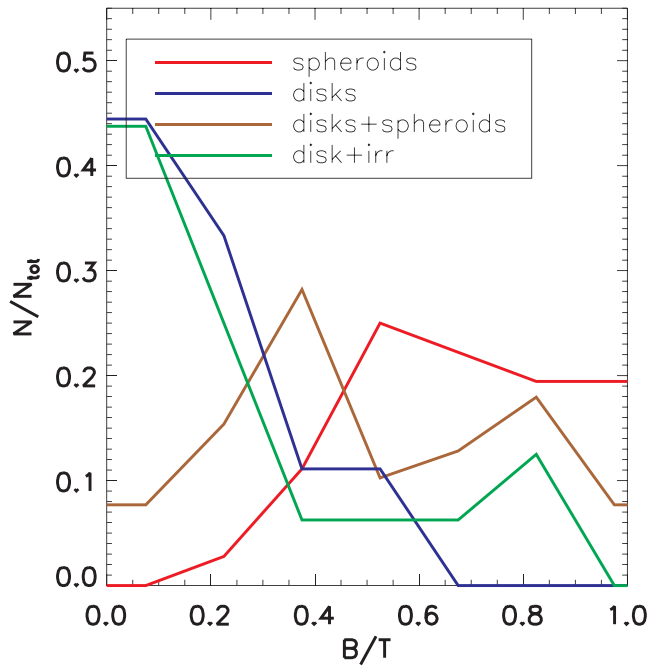


Figure B1. Stellar mass B/Ts for the different morphologies. The visual morphologies defined in this work are compared for some galaxies to the distribution of stellar mass B/Ts. The expected trends are observed.

change with wavelength following a polynomial of order 2. We then fit the seven point SEDs of bulges and discs separately with BC03 templates and estimate the stellar masses of the two components separately. While a detailed discussion of the procedure is beyond the scope of this paper (details are provided in Dimauro et al., in preparation), here we simply want to highlight the fact that the morphologies estimated independently with deep learning do match the expected distribution of B/Ts reasonably well. That is DISCs and

IRRs tend to have bulge fractions smaller than 0.2 whereas SPHs have B/T greater than ~ 0.6 . DISCSPHs have a broader distribution of B/T values. Note, however, that bulge/disc decompositions do not capture the irregularities in the light profile which are an important element in this work.

¹GEPI, Observatoire de Paris, CNRS, Université Paris Diderot, Paris Sciences et Lettres (PSL) Research University, Université Paris Sorbonne Cité, 61 Avenue de l'Observatoire, F-75014 Paris, France

²Department of Physics and Astronomy, University of Pennsylvania, Philadelphia, PA 19104, USA

³Departamento de Astrofísica, Facultad de CC. Físicas, Universidad Complutense de Madrid, E-28040 Madrid, Spain

⁴Harvard-Smithsonian Center for Astrophysics, 60 Garden St., Cambridge, MA 02138, USA

⁵Department of Astrophysics, University of California, Berkeley, CA 94720, USA

⁶School of Physics & Astronomy, University of Nottingham, Nottingham NG7 2RD, UK

⁷Laboratoire AIM, CEA/DSM-CNRS-Université Paris Diderot, Irfu/Service d'Astrophysique, CEA Saclay, Orme des Merisiers, F-91191 Gif-sur-Yvette Cedex, France

⁸Center for Astrophysics and Planetary Science, Racah Institute of Physics, The Hebrew University, Jerusalem 91904, Israel

⁹UCO/Lick Observatory, Department of Astronomy and Astrophysics, University of California, Santa Cruz, CA 95064, USA

¹⁰Space Telescope Science Institute, Baltimore, MD 21218, USA

¹¹School of Physics and Astronomy, Rochester Institute of Technology, Rochester, NY 14623, USA

¹²Department of Physics and Astronomy, Colby College, Waterville, ME 04961, USA

¹³California Institute of Technology, Pasadena, CA 91125, USA

¹⁴Department of Physics and Astronomy, University of Southampton, Southampton SO17 1BJ, UK

This paper has been typeset from a $\text{\TeX}/\text{\LaTeX}$ file prepared by the author.